In: New Trends in Chemical Physics Research
Editor: James N. Lapherty

ISBN: 978-1-61668-535-5

Chapter 1

UNDERSTANDING NANOSCALE PHENOMENA USING SINGLE PARTICLE MASS SPECTROMETRY AND IMPROVEMENT OF ITS PERFORMANCE: A REVIEW

Donggeun Lee[*†a], ***Kwang-Sung Lee***[a‡], ***Sung-Woo Cho***[a§], ***Lei Zhou***[b**], ***Arthur Miller***[c††], ***Kihong Park***[d‡‡] ***and Michael R. Zachariah***[b§§]

[a] Pusan National University, Geumjeong, Busan, Korea
[b]University of Maryland, MD
[c]NIOSH/Spokane Research Lab, WA
[d]Gwangju Institute of Science and Technology, Gwangju Gwangju, Korea

ABSTRACT

Single particle mass spectrometry (SPMS), that is capable of sizing and chemically analyzing single nanoparticles, has offered an opportunity for better understandings of

---

[*] To whom correspondence should be addressed:Tel: +82-51-510-2365, Fax: +82-51-512-5236, Email: donglee@pusan.ac.kr

[†] School of Mechanical Engineering, RIMT, Pusan National University, 30 Jangjeon, Geumjeong, Busan 609-735, Korea

[‡] School of Mechanical Engineering, RIMT, Pusan National University, 30 Jangjeon, Geumjeong, Busan 609-735, Korea

[§] School of Mechanical Engineering, RIMT, Pusan National University, 30 Jangjeon, Geumjeong, Busan 609-735, Korea

[**]Department of Mechanical Engineering, University of Maryland, MD 20742, USA

[††]NIOSH/Spokane Research Lab, WA 99207, USA

[‡‡] Department of Environmental Science and Engineering, Gwangju Institute of Science and Technology, Gwangju Gwangju 500-712, Korea

[§§] Department of Mechanical Engineering and Department of Chemistry and Biochemistry, University of Maryland, MD 20742, USA

mechanisms of aerosol-based nanoparticle synthesis, origin of environmental aerosol particles, and combustion of energetic nanoparticles. Also as ultrafine and accumulation-mode aerosols in the size range of 30 - 300nm can penetrate deeply into human lung and cause serious diseases, the need for advanced SPMS has been rapidly growing. In this article, we therefore offer a broad review of single particle mass spectrometry based on our previous publications, from its working principle and several concerns for interpretation of the data, to the applications for probing nanoscale phenomena,. This article also describes ways to develop and improve the SPMS for better quantification of data and more efficient detection, so as to provide simple design guidelines for SPMS developers.

Keywords: Single Particle Mass Spectrometry, Nano-scale Phenomena, Aerosol, Health Effect, Quantification, Efficient Detection

1. INTRODUCTION

Aerosols play an important role as both a source of environmental/health impact and building blocks to advanced materials. In the latter case, aerosols are synthesized from either gas or liquid phase precursors with the objective of producing particles with desired size (often sub-micrometers or smaller), morphology, and composition. While on-line characterization of size is a well developed method and morphology characterization based on light scattering and electron microscopy has received considerable attention in the last decade, chemical composition determination is still in its infancy. [1] Many such materials are produced by spray-pyrolysis techniques in which liquid droplets containing precursors are injected into a thermal reactor, with resulting evaporation of solvent and reaction of the precursors to form product particles. To have better control in such industrial particle production processes, there is a need to understand aerosol-phase reaction kinetics that govern the final characteristics of product particles. [2]

Metal nanoparticles, for example, aluminum nanoparticles are receiving considerable interest lately as a possible approach to enhance the energy release from energetic materials. It is well known that fine metal particles are highly reactive and in many cases pyrophoric, however, quantification of their reactivity has not been extensively explored. [3,4] Most measurements of condensed-phase reaction kinetics for aluminum particles have been carried out by dynamic thermal techniques such as thermogravimetry (TG) and differential thermal analysis (DTA) that use bulk samples of aluminum nanoparticles. It is well known that those techniques suffer from sampling artifacts associated with mass and heat transfer effects. [5,6] Ideally one would like to explore the intrinsic reactivity of nanoparticles in the absence of other rate limiting kinetic effects associated with heat and mass transfer to clarify what a mechanism is responsible for the reaction kinetics. This would be best achieved by in-situ kinetic measurement of aerosol-phase reaction of a single nanoparticle in air.

Diesel Engines emit a tri-modal size distribution of Diesel particulate matter (DPM) at concentrations as high as 10^9 particles/cm^3. [7] Ultrafine particles i.e. the nuclei- and accumulation-mode particles are known to be the most harmful because of their deep penetration and easy deposition into the human lung. Also coarse-mode DPM often contains alkali and transition metal species such as Ca, Al, Na, Ba, Zn, Fe, Se, Mg and so on. [8] For an efficient removal of such metal-containing particles prior to their emission, one must have the knowledge of contents and size distributions of metal species, and a mechanism of metal formation as well.

Here, we would like to introduce the concept of single particle analysis to address three different research projects of interest that seem to be not easily examined with any conventional characterization tools. If we have an ideal tool capable of sizing and chemically analyzing any single nanoparticle in the aerosol state, the tool may be able to provide key information for understanding the aforementioned physical and chemical nanoscale phenomena. Aerosol time-of-flight mass spectroscopy (ATOFMS or AMS) might be the closest approximation to such a tool. The Prather group reported the simultaneous online measurement of size and molecular composition of single environmental particle using the ATOFMS. [8,9] Recently, we successfully developed an improved Single Particle Mass Spectrometer (SPMS) based on similar principles with the specific goal of addressing such nanoscale phenomena. [6,10-13] During the course of previous research, we have developed and evaluated novel designs of two key components to greatly improve the performance of the SPMS. [15-17]. We also determined how the size of a particle was extracted directly from a mass spectrum signal of the particle. [14] With the help of the design improvements to our SPMS, the three above-mentioned phenomena were successfully investigated.

In this review article, we would like to address the development of the improved SPMS and its applications in regards to our recent research. It will be started in Section II with the brief introduction of the SPMS including a working principle and experimental setup. Section III deals with the three applications of the SPMS as well as several new findings in a view of nanoscale physical chemistry. Section IV is devoted to introduce two designing points to improve the performance of the SPMS.

2. SINGLE PARTICLE MASS SPECTROMETRY (SPMS)

2.1. Working Principle of the Spms

A schematic diagram of the single-particle mass spectrometer (SPMS) used in our study is shown in Fig. 1. The primary components of this system consist of an aerodynamic lens inlet, a two-stage differential pumping system, a free-firing dissociation/ionization laser and optics system, a linear time-of-flight tube assembled with an ion optics and a detector, and data acquisition system composed of a fast, digital storage oscilloscope and a PC. The aerodynamic lens inlet is employed to separate particles from the carrier gas and collimate them to form an aerosol beam. They can be therefore delivered with high efficiency through differentially pumped chambers into the ionization region. The pressure in the chamber which houses both the flight tube and the ionization region is ~ $6\text{x}10^{-7}$ torr when the aerosol inlet is open.

A frequency-doubled pulsed Nd:YAG laser operating at 10 Hz in the internal Q-switch mode is used for ionization of a particle arriving at the ionization region. A 38 mm focal lens mounted internal to the 2nd vacuum chamber focuses the laser beam which intersects the particle beam. The estimated power density with a laser beam diameter of ~0.3 mm and the laser pulse duration of 5 ns is approximately ~ $3\text{x}10^{10}$ W/cm^2 at the focal point. The laser energy is maintained above ~100 mJ/pulse to ensure complete fragmentation and ionization of a single particle as determined by threshold ionization [6]. As configured, positive ions formed by laser ionization are accelerated along ~1 m long linear TOF tube and detected with a microchannel plate (MCP) detector. More complete details of the SPMS are described elsewhere [6,14-17].

Basic instrumentation of the conventional ATOFMS appears to be similar to that of the SPMS. Indeed, the ATOFMS works similarly to some extent. This system however has two significant constraints that are overcome by the current SPMS. First, the ATOFMS employs light scattering techniques for sizing particles as well as triggering the ionizing laser. This approach enables the system to know the time when a particle arrives at the focus of the ionizing laser. Thus, the ATOFMS can provide both size and composition of a single aerosol particle at low concentration. For this reason it is true that the ATOFMS has been a particularly exciting development in the field of environmental research. [8,9,18-20] On the other hand, this benefit is offset by the fact that the measurable size of particles is thus often limited to those larger than 200 nm due to the light scattering limitation. [20] This hinders the use of the ATOFMS to analyze ultrafine particles, which are becoming increasingly more important in various fields such as nanotechnology. Second, the ATOFMS instrument gives the mass spectra comprised of both positive and negative molecular ions. The different polarity of such ions unfortunately facilitates the rapid recombination and charge transfer between the ions. [6,21] This yields some bias in the measured composition of the particle. For this reason, the majority of ATOFMS-based research has focused on reporting qualitative assignment of molecular species in environmental aerosols.

Reents and Ge [21] suggested two simple but very useful approaches to solve the constraints of the ATOFMS. First, they reported that the use of a much stronger laser pulse might solve that problem, because if the beam energy is strong enough to tear a single particle to its constituent atoms and to extract electrons out of those atoms even with a high electron affinity, only positive atomic ions not likely to collide with each other should be produced. As such, the absence of the negative ions would present an advantage i.e. reduced recombination and transfer between ions. They also demonstrated that the measured composition of aerosols was closer to their theoretical value especially in the presence of multiply-charged atomic ions.

Second, they studied the potential of using the ion signal itself from a laser ionization time-of-flight mass spectrometer to estimate particle volume equivalent size. In their work they showed that the total peak area in a single particle mass spectrum can be used to estimate the original particle diameter fairly well within 10 %, even though the number of constituent atoms comprising the particle scatters a lot up to ~34 % depending on particle densities (see Table 1). This shows a good potential accuracy for the estimation of particle size that is not material-dependent.

2.3. Determination of Chemical Composition of a Particle Using Spms

The first version of our SPMS seen in Fig. 1 was developed by adopting their ideas. For characterization of our instrument, we generate NaCl nanoparticles by spray pyrolysis [2,6,23] as a standard material and put them into the SPMS.

Table 1. Size estimation from atomic densities for selected materials with various densities.

Molecular Formula	Molecular weight	Density [g/cc]	No. of atoms in a molecule	No. of atoms / 100 nm sphere	Estimated size [nm]
NaCl	58	2.165	2	$2.35\text{x}10^7$	97
Au(s)	197	19.3	1	$3.08\text{x}10^7$	107
Pb(s)	207	11.34	1	$1.72\text{x}10^7$	88
$(NH_4)_2SO_4$	132	1.769	7	$2.95\text{x}10^7$	105
$(NH_4)HSO_4$	115	1.78	6	$2.92\text{x}10^7$	105
$C_{20}H_{42}$	282	0.789	20	$1.76\text{x}10^7$	88
SiO_2	60	2.65	3	$4.17\text{x}10^7$	118
Al(s)	27	2.7	1	$3.15\text{x}10^7$	107
Al_2O_3(s)	102	4	5	$6.17\text{x}10^7$	134
C_8H_8(s)	104	1.05	8	$2.54\text{x}10^77$	100
Fe(s)	56	7.86	1	$4.42\text{x}10^7$	120
			Average[a]	$(3.2\pm1.3)\text{x}10^7$	106±14

[a] The smaller deviation for the average particle size comes from the calculation of the diameter using the cube root of the number of atoms.

An example of a typical mass spectrum for a single sodium chloride particle of nominal diameter ~70 nm is shown in Fig. 2. With the laser fluencies used we never observe any multi-atomic species, while multiply-charged atomic ion peaks are usually observed, and indicate that ionization efficiency is high. In addition to the signals for Na and Cl, we also see H and O presumably from our inability to completely dry the aerosols. In our prior work we demonstrated that under these conditions, relative ion concentration could be determined to within 15% for a variety of different aerosols [6].

The formation of multiply-charged positive ions is not surprising when one considers a simple estimation of the minimum threshold energy required for disintegration/ionization of a NaCl nanoparticle. The minimum energy required to convert a 100 nm NaCl particle into Na+ and Cl+ is $6\text{x}10^{-14}$ J. For the laser power density discussed above (100 mJ/pulse) the nominal energy a 100 nm diameter particle is exposed to is $1.1\text{x}10^{-8}$ J (see also table 3 in Reents and Schabel [22]), or > $5\text{x}10^6$ times higher than the minimum threshold energy.

Elemental stoichiometry ratios evaluated for 168 sodium chloride particles are indicated in Fig. 3. The mode for the atomic sodium fraction (Na / (Na+Cl)) is at 0.516, which is very close to the theoretical value of 0.50. A further indication of the ionization efficiency is the invariance in the signal intensity, for 70 nm NaCl particles and 85 nm Al particles (DMA selected) with increasing laser power [14]. Above ~50 mJ/pulse no increase in ion intensity is observed indicating that the ionization process has been saturated. The results presented in Figures 2 and 3 are highly indicative that the ionization process, under the experimental conditions described here, is highly efficient.

2.4. Size Estimation of a Particle Size from its Mass Spectrum

Particle size estimation suggested by Reents and Ge [21] can be justified when two necessary conditions are satisfied. The first condition is “complete ionization”, where all constituent atoms are converted to ions. As explained in the previous section, this condition is presumably satisfied with the use of extremely high laser fluencies [21,22] The second condition is that all ions generated through the complete ionization should be delivered from the laser ablation/ionization region to a detector with no traveling loss. When these two conditions are met, the ion signals in a mass spectrum will reflect the total number of atoms comprising the parent particle ($\propto$ volume of particle) and the integrated signal intensities should have a linear relation to the particle volume. However, the cube root of the integrated ion current for various particle diameters (50, 70, 120, 150 nm) selected from the DMA is not linear as seen in Fig. 4. The possible reason for the nonlinearity will be explained in the next section. Instead, here we would like to emphasize that the correlation, regardless of the nonlinearity, is not material dependent. This implies that this correlation can still be used for proper estimation of particle size with unknown composition.

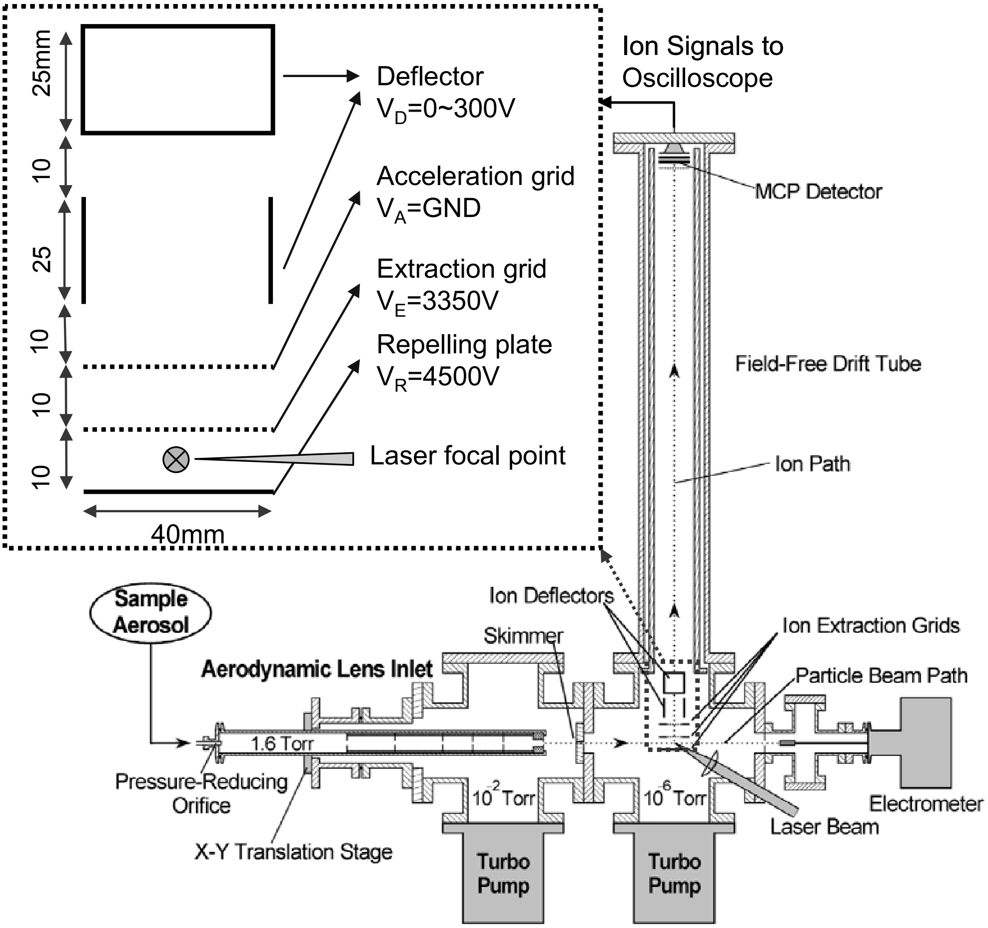

Figure 1. A schematic of the single particle mass spectrometer and a detail configuration of the ion optics.

Using the relationship in Fig. 2, we obtain a size distribution of size-polydisperse NaCl particles from more than 1000 mass spectra. For comparison, a commercial scanning mobility particle sizer (SMPS) is used to measure the size distribution of the same aerosols. Fig. 5 shows good agreement between the very different approaches to obtain particle size. For presentation purposes, the height of the SMPS size distribution is rescaled to match the SPMS-estimated size distribution. The result indicates that now we are ready to use the SPMS to obtain quantitative measurements of size and atomic composition of any aerosol particles.

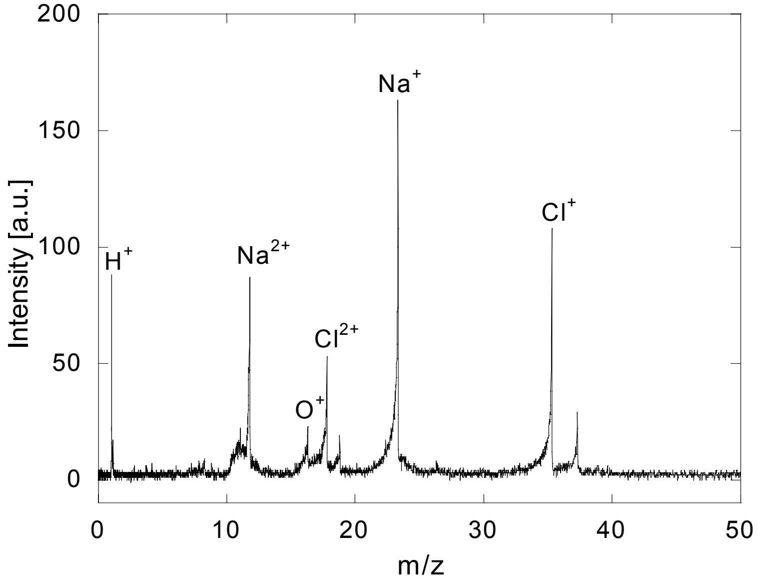

Figure 2. Typical mass spectrum of a NaCl nanoparticle (~70 nm).

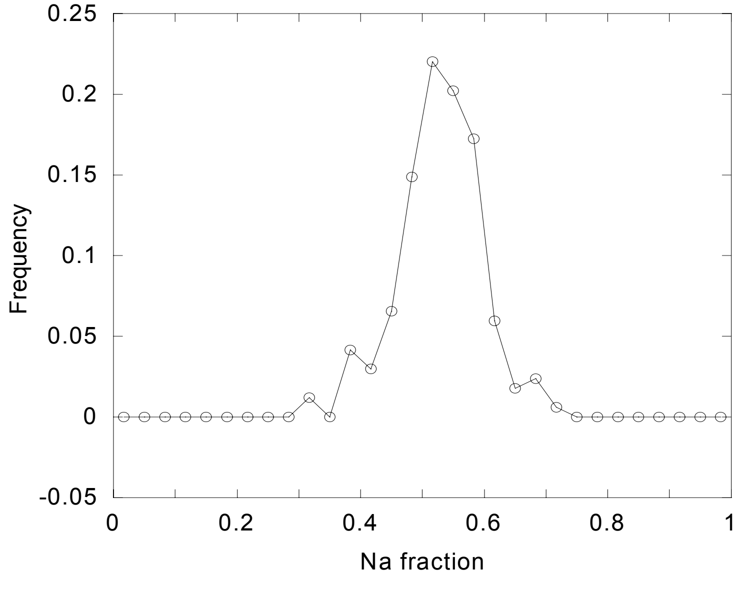

Figure 3. Histogram of Na fraction in polydisperse NaCl nanoparticles.

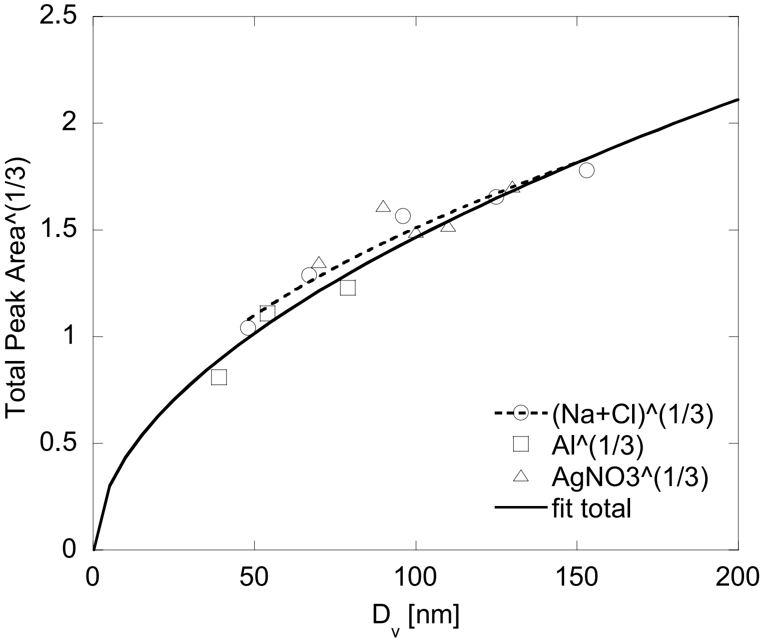

Figure 4. Non-linear relationship between the cube root of integrated ion signal intensity and particle size.

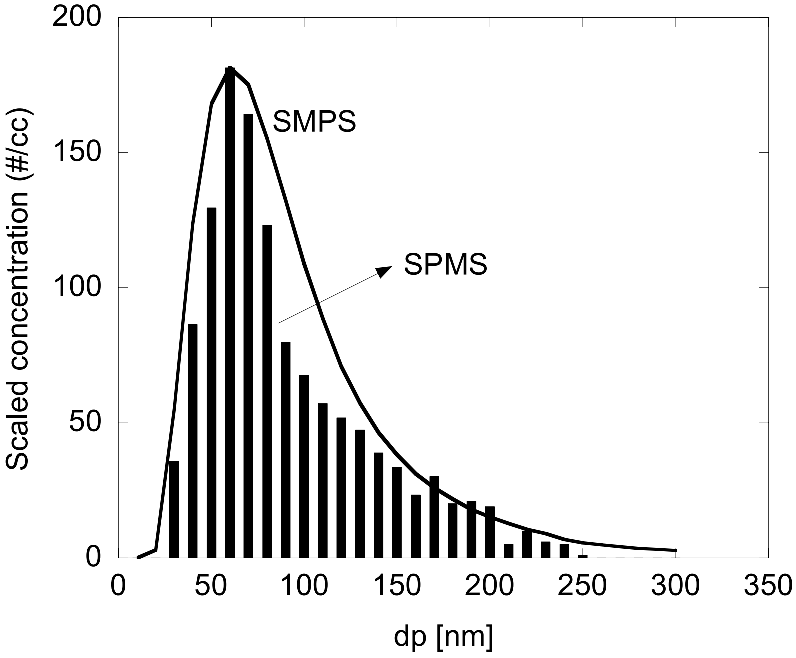

Figure 5. Comparison of size distributions measured by SPMS and Scanning Mobility Particle Sizer.

2.5. Transport Losses of Energetic Ions

Section of II-2 and II-3 described that such a strong laser pulse generates positive ions only. Under the voltage setup in Fig. 1, negative ions and electrons even if any exists can not be detected. To test this, inverse negative voltages were supplied to the repelling plate and extraction grid so as to ensure the non-existence of the negative ions. The experiment revealed that electrons are the only negatively-charged species. Taking this into account, the following simple model is developed to describe Fig. 4.

We first assume that the laser–particle interaction converts a particle into a spherical ion cloud of positive ions with a uniform charge density. The positive ions then undergo expansion due to hydrodynamic and Coulomb repulsion [24]. Ions initially located at the surface will be repelled by all inner charges and internal pressures from the developed plasma, with the outer atoms having the maximum possible kinetic energy (KE), and with the largest population as compared to the inner ions. When particles of different sizes are converted into their respective ion clouds, under the assumption of a constant cloud density, the cloud size is to first order proportional to original particle size. [24,25] Based on this, the KE of outer-surface ions dominates the mean KE and one might assume the KE may relate indirectly to the parent particle surface area ($KE \propto d_p^2$). In other words, larger particles might generate the more energetic ions.

At this moment it is interesting to investigate the origin of the nonlinearity. Following the energetic ion creation, some ions will arrive at the detector, while others can be lost at the TOF wall. The relative loss of total ions is first explored as a function of ion kinetic energy. The upward-ejected ions in Fig. 1 will be detected regardless of their initial kinetic energy and they will have the shortest time of flight. Backward-ejected ions decelerate and turn back to the MCP due to the electric field in the extraction region. Thus, the backward-ejected ions continue to be detected and have the longest time of flight. In contrast, horizontally ejected ions are most likely to collide with the inner wall of TOF tube and never make it to the detector. As the ejection angle with respect to the TOF upward axis increases, it becomes more difficult to detect the ions. Thus, it is possible to build a model to determine a certain range of the detectable angle at which ions depart. The two maximum detectable angles are in the proximity of both 0^o and 180^o. As all ions between these two maximum angles are lost, we would say that "a cone of silence" exists.

The trajectories of ions are simulated by using the commercial software SIMION. Fig. 6 shows the trajectories of Na^+ ions when they are ejected in all directions at four different kinetic energies. The voltages V_R, V_E and V_A are set for space focusing with values of 4500, 3350 and 0V, respectively as noted in Fig. 1. In the conventional plate-type ion optics, it is clear that a higher KE leads to greater ion loss. Fig. 7 shows a more quantitative explanation of this effect. Detection efficiency (DE), defined as the ratio of the number of ions arriving at the detector to the total number of ions emitted, is estimated at each specified KE. DE is highly KE-dependent, inverse-proportional to KE over a wide range ($DE \propto KE^{-1}$). Substitution of the aforementioned $KE \propto d_p^2$ into the relationship of $DE \propto KE^{-1}$ results in the reduced form of $DE \propto d_p^{-2}$. Hence, the bigger the particle size, the greater the ion loss is. This explains the size-dependent deviation from a linear line representing 100% detection of ions.

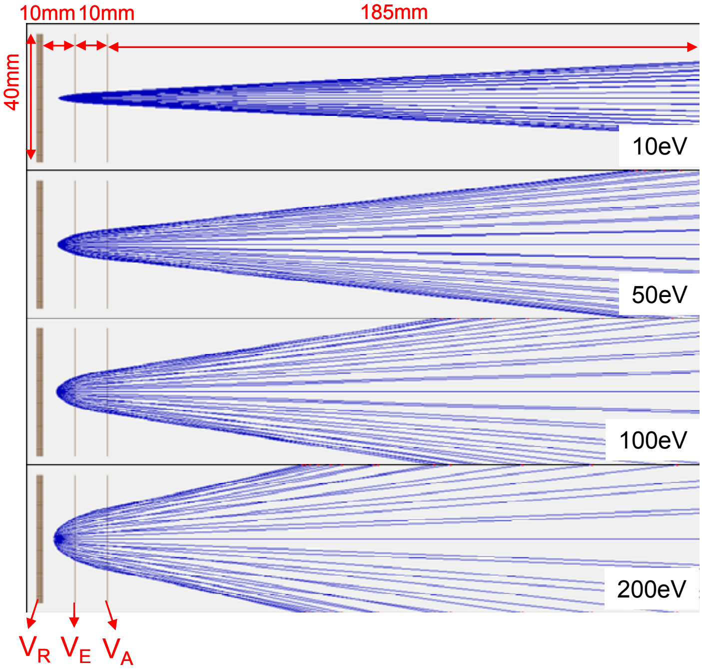

Figure 6. Trajectories of Na^+ ions launched at four different KEs in the three different E-field regions of extraction, acceleration, and field-free TOF regions.

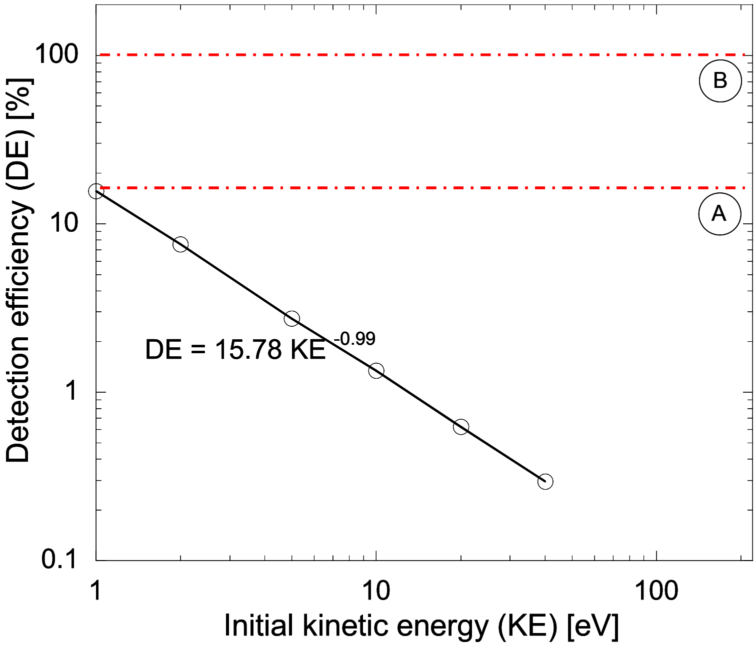

Figure 7. Profile of detection efficiency against the initial kinetic energy of ions in the conventional ion optics.

2.6. Nanosecond Laser-Induced Energetic Ion Formation

In this section, we will discuss in more detail the size-dependent energetic ion formation. A molecular dynamic simulation is used to investigate this. We postulate that positive ions generated by a nanosecond high-power laser pulse form a spherical ion cloud, which has often been adopted for the breathing sphere model [26]. The spherically symmetric system makes the calculation much simpler.

It has been observed that very energetic positive ions up to 1 MeV are formed when a femto-second laser pulse deposits a gas cluster [26,27]. The dynamics and maximum kinetic energy of the ions were predicted qualitatively well by Ditmire et al.'s nanoplasma model [26]. Note that the femto-second laser pulse has an extremely large intensity (> 10^{15} W/cm^2), which implies that even at the beginning of the pulse, enough electrons exist for collision ionization in a spherical plasma cloud. Collision ionization increases the electron density rapidly, often up to more than the critical value. The highly dense electrons in a nanoplasma ball are heated resonantly by the surrounding laser field, leading to a very rapid expansion of the plasma ball. A theory including tunneling, collision-induced ionization, and subsequent nanoplasma resonance with the pulse seem very likely to be accepted by the research community.

In contrast, the majority of nanosecond lasers used for the SPMS have a much lower intensity, typically less than 10^{10} W/cm^2. This intensity seems to be insufficient to generate electrons to such a high density. Therefore, resonant heating of the plasma ball may not occur, in turn, the above-mentioned hydrodynamic expansion may not be the case. Indeed, single-photon or multi-photon ionization of clusters or gas molecules with nanosecond laser pulse at low-to-moderate intensities has been studied, and the photofragmentation [28] and Coulomb explosion [29] dynamics have been proposed as the corresponding mechanism. The kinetic energy (KE) of the ions at those intensities was revealed to be much less than in the former case.

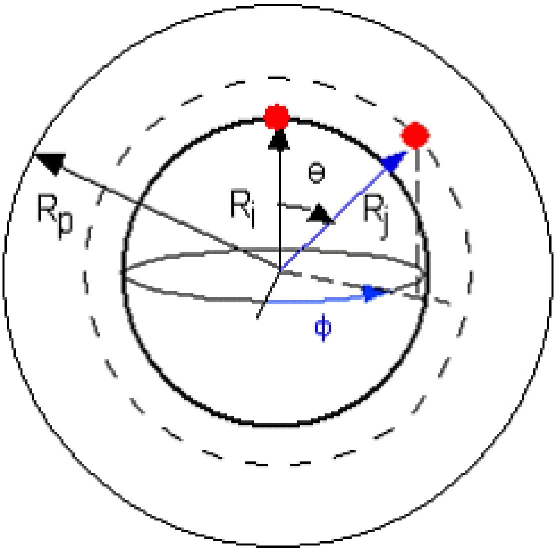

Figure 8. Spherical coordinate system for an ion cloud.

Together with contradictions in the mechanism, whether the cluster can be treated as plasma or not has given rise to a controversy. For example, classical dynamics simulations including the Coulomb field of the ions indicate that the electrons are quickly removed at the beginning of the interaction even from large clusters. [25] That makes the nanoplasma model [26] questionable. A thing to note is that all the above discussions are only for gas clusters, not for nanoparticles. There are no available experimental data for nanoparticle ionization. Are we between a nanoplasma ball and a positive ion cloud, or hydrodynamic and Coulomb expansion? Unfortunately, we are not currently in a position to answer that question. Regarding our conditions, for ionization of a nanoparticle by a longer (5 ns) much weaker (~10^{10} W/cm^2) laser pulse, the condition should lie between the above two limiting cases.

Therefore, we first choose the simplest model the main assumption of which is as follows. Particles are completely ionized to yield positive ions which form a spherical cloud. The interaction of each pair of ions is depicted by Coulomb repulsion. Fig. 8 shows the coordinate system, where R_i and R_j denote the radial position vectors of the i_{th} and the j_{th} ions as

$$\vec{r}_{ij} = r_j \sin\theta_j \cos\phi_j \hat{i} + r_j \sin\theta_j \sin\phi_j \hat{j} + (r_j \cos\theta_j - r_i)\hat{k} \tag{1}$$

First, we derive the differential force vector d^3F_{ij} exerted on the i^{th} ion by the j^{th} ion by differentiating the corresponding Coulomb potential U_{ij}

$$U_{ij} = \frac{1}{4\pi\varepsilon_0}\frac{q_i q_j}{r_{ij}}, \quad d^3\vec{F}_{ij} = -\nabla U_{ij} = \frac{1}{4\pi\varepsilon_0}\frac{q_i q_j}{r_{ij}^{\ 3}}\vec{r}_{ij} \tag{2}$$

where q_i and q_j are ionic charges of the i^{th} and j^{th} ions, respectively and ε_0 is vacuum permittivity. Net force on the i^{th} ion by all surrounding ions is directed upward due to the symmetry and is obtained by integrating the above d^3F_{ij} as

$$\vec{F}_i = \iiint d^3\vec{F}_{ij} \cdot \hat{k} = \frac{\rho^2 V_0}{3\varepsilon_0} r_i \tag{3}$$

where ρ and V0 are constant charge density of ions in the ion cloud and volume of the cloud, respectively. Thus the ionic charge is given by qi = ρdVi. The potential energy on the ith ion is also obtained by integrating the above Uij over all jth ions as

$$U_i = \frac{1}{4\pi\varepsilon_0}\iiint \frac{\rho^2 V_0}{r_{ij}} r_j^{\ 2} \sin\theta_j d\theta_j d\phi_j dr_j = \frac{\rho^2 V_0}{12\varepsilon_0}(3R^2 - r_i^{\ 2})) \tag{4}$$

where R is outer diameter of the spherical ion cloud. The total potential energy for the whole ion cloud U is given by integrating Ui against the volume as

$$U = \iiint U_i 4\pi r_i^2 dr_i = \frac{4}{15}\frac{\pi}{\varepsilon_0}\rho^2 R^5 \tag{5}$$

Mean total potential energy is obtained by dividing the U by total number of ions Ns as

$$\overline{U} = \frac{U}{N_s} = \frac{3Ue}{\rho 4\pi R^3} = \frac{\rho R^2}{5\varepsilon_0} \tag{6}$$

This is the first explicit expression for the size dependency of the potential energy of ions. The potential energy is completely converted into kinetic energy after sufficient time. Thus, Eq. 6 obviously shows that a larger particle or ion cloud leads to a higher potential and kinetic energy. As predicted in Section II-5, the mean kinetic energy of the ions in Eq. 6 is proportional to the surface area of the original particle. Interestingly, the previous experiment showed a 1.6th power for the R dependence [14], which is fairly close to the second power of R in Eq. 6. That proximity supports that the energetic ions may form through Coulomb repulsion.

Despite the fairly good agreement, it should be noted that the Coulomb repulsion model is derived under the assumption that the positive ions begin to expand in the absence of any electrons. All electrons escape from the ion cloud prior to the expansion. It is partly true in particular at the early stage of multi-photon ionization where electrons undergo less attraction. As more electrons depart from the cloud, the net charge of the ion cloud increases, forcing electrons to stay around positive ions. This seems to say the system is in the proximity to the nanoplasma, i.e. no electron escape. The caged electrons are then heated presumably by coherent electron motion [30] or resonant laser-electron coupling [26,31,32] either of which was proposed for the system of femto-second laser ionization of gas clusters. Such laser-driven hot electrons collide with atoms and/or ions, yielding multi-charge ionization, i.e. inverse Bremsstarhlung and at the same time expand rapidly with drawing out the surrounding ions. As both electrons and ions expand far enough, electrons exceeding Coulomb potential begin to escape, transforming the plasma sphere into the positive ion cloud. This is the time for Coulomb expansion, but generating less energetic ions as compared to the case of the pure Coulomb expansion model. Hence, the nanoplasma would be another limiting case of current system.

Here, we employed the 1-D hydrodynamic code based on a one-fluid two temperature (a single component particle; electron and ion temperature), which includes thermal conduction, a collision-radiative model for the ionization dynamics, the complete details for which are presented elsewhere [31]. From our prior simulations [32], we found the energetic ions are produced through two successive processes: 1) soft heating regime where single Al particle is evaporated to form a spherical fume 2) transition to a resonant absorption and hydrodynamic plasma expansion. During the expansion, electrons are highly non-uniformly distributed in radial direction, so that the surface electrons are first resonantly interacted with and heated very rapidly by the laser pulse. Interestingly, kinetic energy profile as a function of radial position R is pretty similar to Eq. 4 (see Fig. 5(a) in reference [32]). Moreover, we found that as particle size increases, the average kinetic energy as well as the maximum kinetic energy increases, following a similar power law relationship (KE ~ dp1.43). Totally different theories for the two limiting cases give similar results.

3. APPLICATIONS OF SINGLE PARTICLE MASS SPECTROMETRY

In this section, we would like to demonstrate that the ability of SPMS goes beyond just measurement of size and composition of particles when it is applied to studies on the three aforementioned nanoscale phenomena on the basis of our previous researches [6,10-12].

3.1. Kinetic Measurement of Aerosol-Phase Spray Pyrolysis Reaction

Spray Pyrolysis Reaction

Fig. 9 shows the setup for production of particles by spray pyrolysis. A solution of nitrate, typically of 1 wt %, is prepared by mixing a kind of commercially available metal nitrate (> 99 % in purity) with filtered deionized water and atomized in air to generate aerosol droplets of the solution. The droplet-laden air is then passed through an aerosol dryer filled with dry silica gel to remove most of the water content in the droplets (say drying). After the solvent evaporates out of the droplet, the remaining salute forms a solid particle the size of which is controlled by the initial concentration of solute in the solution. The metal nitrate particles are delivered into a tube heated in a tube furnace. The heating decomposes metal nitrate particle into solid metal oxide and nitric oxide gas leaving the solid (say pyrolysis) according to

$$\mathrm{Al(NO_3)_3} \rightarrow \alpha\mathrm{Al_2O_3} + (1-\alpha)\mathrm{Al(NO_3)_3} \rightarrow \mathrm{Al_2O_3} + 3\mathrm{NO_2(g)} \qquad (7)$$

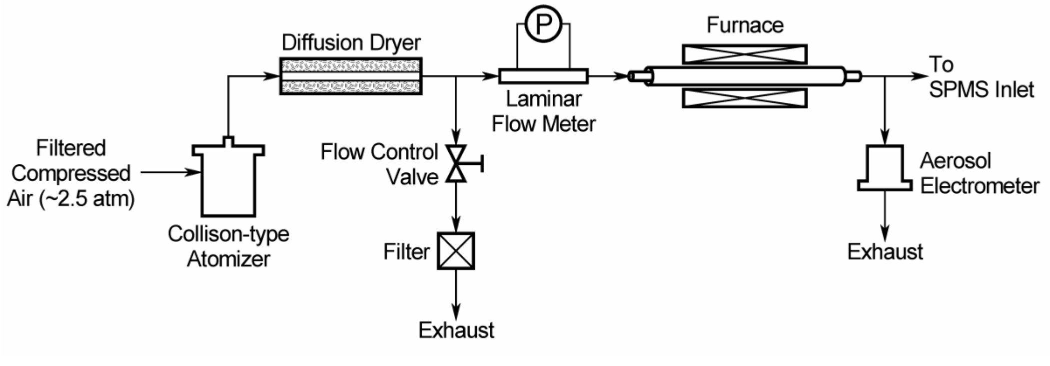

Figure 9. Schematic of the aerosol generator and thermal reactor setup

This is why this reaction is called spray pyrolysis.

The output aerosol from the furnace is split into two streams, one which is delivered to the SPMS and the other for monitoring the aerosol concentration with an aerosol electrometer. By analyzing the relative peak area of each element of the aerosol, the mass spectrometer can provide the stoichiometry ratios of O/Al, N/Al, and N/O at varied temperatures. At 100 °C as seen in Fig. 10, the ratio of nitrogen to aluminum is about 2.7 (expected stoichiometry of 3:1) while oxygen to aluminum ratio was ~8.3, and reflect that reactant particles are just starting to decompose. For calculation of the O/Al and N/O ratios at low temperatures, the oxygen contribution due to the presence of water, which was described earlier, is taken into account. Reduction of the nitrogen fraction, found in both N/Al and N/O, reveals progress of nitrate decomposition at higher temperatures. At 800 °C, the reaction seems to have completed, and the O/Al ratio reaches ~1.5 which corresponds to the theoretical stoichiometry of aluminum oxide, while the nitrogen fraction approaches a negligible level.

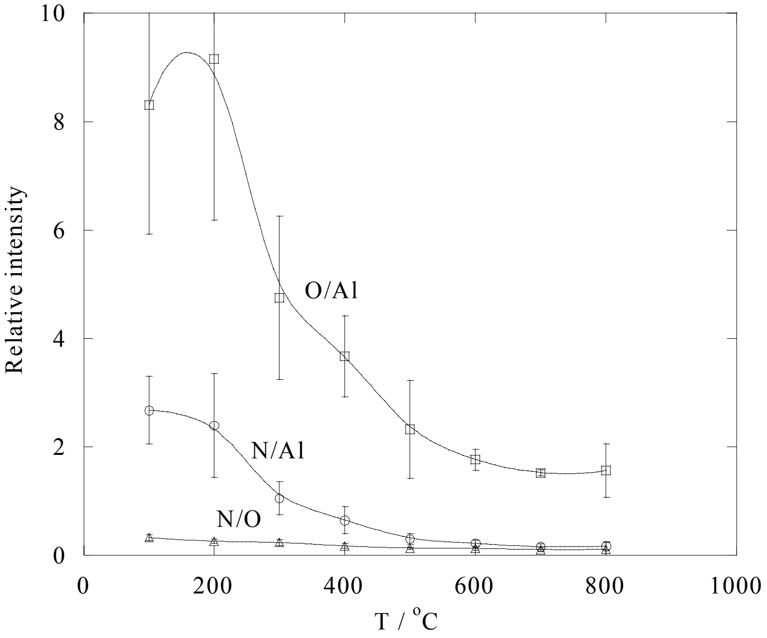

Figure 10. Change in relative intensities of nitrogen, and oxygen, and aluminum ion peaks during thermal decomposition of aluminum nitrate ($Al(NO_3)_3$).

Measurement of Kinetic Data of the Spray Pyrolysis Reaction

The extent of conversion, $\alpha \equiv (w_0 - w)/(w_0 - w_f)$, where w is the sample mass and the subscripts 0 and f represent the initial and final states of the reaction, respectively, could be calculated using the atomic fraction of nitrogen in particles <N> under a certain condition

$$\langle N \rangle = \frac{N}{Al + N + O} = \frac{1}{[Al/N] + 1 + [O/N]} \tag{8}$$

The extent of mass conversion α is found to be the same as the extent of mole conversion in Eq. 7. Fig. 11 provides a plot of the extents of conversion obtained for four metal nitrates (aluminum, calcium, silver, and strontium) at different reaction temperatures. Silver and aluminum nitrates exhibit lower decomposition temperatures (~200 °C for $\alpha = 0.5$) whereas the 50% conversion is observed at about 650 °C for calcium and strontium nitrates.

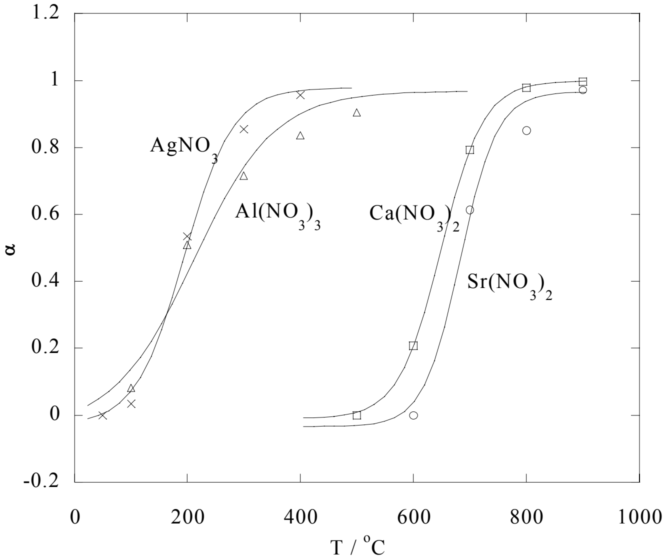

Figure 11. Temperature dependence of the extent of conversion obtained by SPMS for four metal nitrates.

The mathematical expression used for the kinetic parameters [6] is addressed as follows. Most condensed-phase reactions studied by traditional thermal analyses have been described using the following equation

$$\frac{d\alpha}{dt} = k(T)f(\alpha) \tag{9}$$

where k(T) is the reaction rate constant that is temperature-dependent, and $f(\alpha)$ is a mathematical representation of the reaction model. We assume a single-step first-order reaction for thermal decomposition of metal nitrates throughout the study, in which case $f(\alpha)$ is equal to $1-\alpha$. [33]

Eq. 9 can be written in an integrated form as

$$g(\alpha) \equiv \int_0^\alpha \frac{d\alpha'}{f(\alpha')} = \int_0^t k(T)dt' \tag{10}$$

where $g(\alpha)$ is equal to $-\ln(1-\alpha)$ under the first-order reaction assumption [33]. For the SPMS experiment, we assume an isothermal reaction, and thus k(T) is constant with respect to the time. For our analysis, a plug-flow tube reactor model is used. Thus, the reaction duration time t is estimated by dividing the 30cm-long reaction zone volume by the volume flow rate which is 1.0 l/min measured at room temperature. The time t is on the order of a second at room temperature. At higher temperatures, the volume flow rate change is considered assuming the ideal gas law, and the reaction duration time is adjusted for analysis. By applying the Arrhenius relationship for k(T), Eq. 10 yields

$$\ln(g(\alpha)/t) = \ln k(T) = \ln A - \frac{E}{R}T^{-1} \tag{11}$$

Therefore, by repeating the measurement at various temperatures and determining corresponding extents of conversion, the activation energy and pre-exponential factor are obtained from an Arrhenius plot. The mathematical expression is essentially the same as used in conventional thermogravimetric analysis (TGA) [33,34]. Eq. 11 shows the relationship among α, k(T), and the Arrhenius parameters, i.e. the activation energy (E) and pre-exponential factor (A). The decomposition reaction is assumed to be single-step and first-order, and the heating process is approximated to be isothermal. Results are shown in Fig. 12. Each nitrate exhibited good linearity, which implies the single-step first-order assumption and use of the Arrhenius relationship are appropriate, although the number of points in the plots is limited.

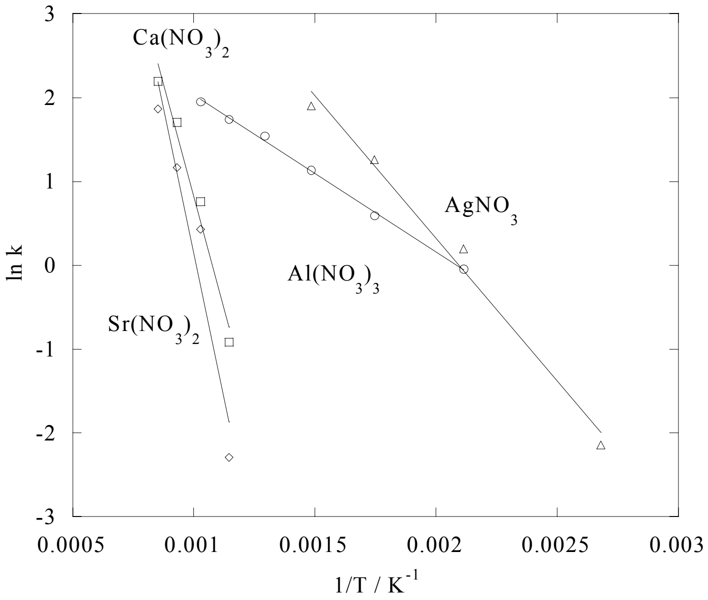

Figure 12. Arrehenius plot of for thermal decomposition of metal nitrates produced from obtained by SPMS data.

Change in Reaction Kinetics with Decreasing Initial Sample Mass

An important observation is to note that the reaction in the aerosol phase is taking place much faster than in the bulk powder state such as in a TGA dish. In Fig. 13, the Arrhenius plots obtained by SPMS and by dynamic TGA with the varied initial sample masses are shown together for calcium nitrate decomposition. The reaction rate constants for the TGA results are calculated by

$$\frac{d\alpha}{dT} = \frac{k(T)}{\beta} f(\alpha) \tag{12}$$

With an assumption that the term dα/dt can be expressed as the product of dα/dT and dT/dt, and defining a constant β be equal to dT/dt (the heating rate). We used this transformation which has been widely used in kinetics studies with conventional dynamic thermal techniques, although it has been criticized. [33] The curves for TGA in Fig. 13 show that the extent of conversion ranges from 0.1 to 0.9. The temperature ranges in which the rate constants are obtained by the two techniques do not overlap with each other. This is because there is a difference between the two techniques in the dynamic range for reaction rate measurement for a given temperature. The increase of the apparent reaction rate in TGA for decreasing mass is clearly demonstrated in this figure. As the mass decreases, it is interesting to note that the reaction rate constant determined by TGA moves up toward that derived using the SPMS. However, even with the smallest sample mass used in TGA (1.33 mg), there is a significant gap between TGA and SPMS, and the difference is approximately an order of magnitude at 600 °C. The initial sample size also affected the curve shape in the Arrhenius plot. For example, the Arrhenius curve has a straight line shape for the cases of the initial masses equal to or smaller than 2.29 mg. This usually indicates that the reaction model (single-step first-order) and Arrhenius relationship work quite well altogether for this reaction system. On the other hand, the Arrhenius curve has a non-linear structure when the initial sample mass was 7.45 mg or greater, and the same processing technique appears to have failed. This is another example of the initial mass effect that plagues reaction kinetics studies using TGA.

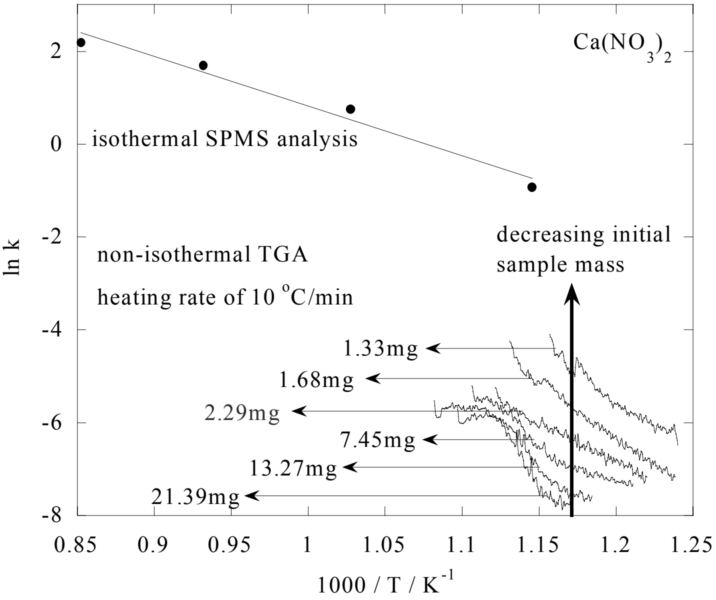

Figure 13. Comparison of the reaction rates of calcium nitrate obtained by SPMS and by conventional TGA. Note the upward shift of the reaction rate in the TGA results for smaller initial sample masses.

Discrimination of the causes of mass-loading on the observed kinetics in TGA is very difficult if not impossible to assess. The variety of potential mass-loading effects can range from simple heat capacity effects resulting in different actual heating rates for different sample sizes, to more complex phenomena. These might include longer diffusion paths for products of reaction for bulk samples. In the case of interest here, these might be evolution of NO or NO_2, where the observed kinetics would result from a slower mass loss rate, or the fact that the lowered loss rate of the NO_x results in a shift in the equilibrium constant as discussed by Ettarh and Galwey [35]. In general, however, the observed increase in the apparent rate constant as the sample size decreases implies that in the limit of very small sample sizes we should be observing rate behavior that is uncorrupted by these other transport related effects. Nevertheless, we feel confident therefore that our chemistry is not affected by any new phenomena that occurs at the nanoscale.

3.2. Size-Resolved Kinetic Measurement of Aluminum Nanoparticle Oxidation

Aluminum nanoparticle aerosols of various characteristics are generated by three different methods: DC arc discharge, laser ablation, and aerosolization of pre-made commercial aluminum powder. The resulting aerosols are fed into a tube furnace maintained at varied temperatures so as to react with air and are then injected into the SPMS as described in the previous section. Details of the aerosol generation are described elsewhere [10]. In this section, we will describe how the SPMS is used to obtain the size resolved oxidation rate of aluminum nanoparticles in air and to describe what the mechanism for the combustion is.

Kinetic Measurement of Aluminum Nanoparticle Oxidation

We first obtain isothermal kinetic data for DC arc-generated aluminum nanoparticle oxidation by passing particles through the tube furnace for a given residence time (~1 s) and temperature (25 °C ~ 1100 °C), and subsequently sampling with the SPMS. The SPMS-determined atomic fractions of aluminum (Al/(Al+O)) for 200~300 particles at a given temperature are used to estimate the extent of conversion α as defined by Levenspiel [36], i.e.

$$\alpha = \text{volume of converted material / total volume of particle.} \qquad (13)$$

Thus, if the α equals one, a particle is completely oxidized to aluminum oxide (Al_2O_3), while the value of zero indicates the particle is pure aluminum. Values between 0 and 1 indicate a partially oxidized particle having the internal structure of an unreacted core (Al) surrounded by an aluminum oxide shell. Using the atomic fraction and size of an aluminum particle and size estimated from single measurement by SPMS, we can calculate the extent of conversion as a function of particle size at each temperature. The same mathematical expressions described in Section III-1 are used again to obtain the kinetic data, but as a function of particle size. In order to obtain a kinetic rate constant from the data, however, one must first propose a suitable model for $f(\alpha)$ and/or $g(\alpha)$ in Eqs 9-11. We choose the well known idealized “shrinking core” model for spherical particles of unchanging size [36] to describe aluminum nanoparticle oxidation. This process is repeated for three other sorts of aluminum particles, i.e. generated by the laser ablation and by the aerosolization of two commercially available powders.

Table 2. Summary of kinetic parameters of four sorts of aluminum nanoparticle oxidations.

Generation Method	Mean primary particle size[a]	Peak mobility size[b] (mode diameter)	Temperature	Fraction of completely oxidized particles
DC Arc discharge	~ 19 nm	~ 65 nm	900 °C	~ 68%
Laser ablation	~ 23 nm	~ 75 nm	1100 °C	~ 57%
Nanopowder (Aveka)	~ 29 nm	~ 70 nm	1100 °C	~ 13%
Nanopowder (Nanotechnologies)	~ 50 nm	~ 160 nm	1100 °C	~ 4%

[a] The mean primary particle size was measured using the TEM images.

[b] The peak mobility size was measured with the scanning mobility particle sizer (SMPS).

Table 2 summarizes the results of characterization and oxidations of the four different aluminum particles. For example, as temperature increased, the fraction of particles with $\alpha = 1$ (i.e., Al_2O_3) increases, and at 900 °C, ~68 % of the DC arc-generated Al nanoparticles are completely oxidized to Al_2O_3. It is notable that the smaller particles oxidized first (i.e. for any given temperature, smaller particles have a larger extent of conversion). For the two kinds of Al particles with smallest primary particles (highest reactivity), i.e. DC Arc-generated and Laser ablated Al particles, each data set is binned by three size ranges (< 50 nm, 50-100 nm, and 100-150 nm). For these two particle types, Arrhenius parameters (activation energy and pre-exponential factor) are obtained using the size-resolved reaction rate constants as a function of temperature from Arrehenius plots (ln (k) versus 1/T), similar to the approach demonstrated in Figs. 12 and 13. We should note that with decreasing particle size, the rate constant increases and the activation energy decreases as summarized in Table 3. It is consistently observed that the activation energy decreases with decreasing particle size (agglomerate size). We hypothesize that the decreased reactivity with increasing the agglomerate size is caused by decreased particle surface area-to-volume ratio as the mobility size increases. Since the aluminum particles are agglomerates with some extent of “necking” or coalescing spheres (refer to TEM images in Fig. 10 of the reference [10]), the surface area-to-volume ratio should decrease as the agglomerate size increases. Only agglomerates with a point contact among primary particles have the constant surface area-to-volume ratio, independent of agglomerate size.

A Mechanism of Aluminum Nanoparticle Oxidation

The shrinking core model involves a reaction front moving radially inward and separating an unreacted core from a completely reacted ash outer layer. The overall reaction is believed to occur in the following three successive steps:

Step 1: Diffusion of gaseous reactant (oxygen) through the film surrounding the particle to particle surface (film resistance)

Step 2: Diffusion of gaseous reactant (oxygen) through the ash (oxide shell) to the surface of unreacted core (aluminum) (ash resistance)

Step 3: Chemical reaction of gaseous reactant (oxygen) with solid (aluminum) at unreacted core surface (chemical reaction resistance)

Since a solid ash (oxide shell) forms very rapidly when the particle is exposed to air, the first step (film resistance) can be ignored as a rate limiting step (i.e., the ash resistance is much greater than the film resistance). The time for complete conversion in each limiting step can be described by [10,36]

Table 3. Summary for Arrehenius parameters for aluminum nanoparticle oxidations.

Generation Method	Particle mobility size	Temperature range	Activation Energy (kJ/mol)	Pre-exponential factor (1/sec)
DC Arc discharge	< 50 nm 50-100 nm 100-150 nm	600~900 °C	31.8 56.9 174.6	$2.4*10^1$ $1.8*10^2$ $5.4*10^7$
Laser ablation	< 50 nm 50-100 nm 100-150 nm	800~1100 °C	24.6 104.8 120.2	$3.5*10^0$ $5.0*10^3$ $4.4*10^3$

$$\frac{t}{\tau_{diffusion}} = 1 - 3(1-\alpha)^{2/3} + 2(1-\alpha),\ \tau_{diffusion} = \frac{\rho_{Al} D_p{}^2}{32 D_e C_{O_2,\infty}}$$

: Diffusion controlled step

$$\frac{t}{\tau_{reaction}} = 1 - (1-\alpha)^{1/3},\ \tau_{reaction} = \frac{\rho_{Al} D_p}{8/3 k_s C_{O_2,\infty}}$$

: Chemical reaction controlled step (14)

where t is the reaction time, ρ_{Al} is the molar density of aluminum, D_e is the effective diffusion coefficient of oxygen through the ash layer, $C_{O2,\infty}$ is the oxygen molar concentration in gas, D_p is the particle diameter, and k_s is the first-order rate constant for the surface reaction.

To determine the rate limiting step, we also measure the extent of conversion by adjusting the reaction time (t) (i.e., the residence time in the furnace reactor) for a given temperature. By fitting each model (Eq. 14) to our experimental data (t vs α), we can infer the likely limiting step. Fig. 14 plots our experimentally determined reaction time (t) and extent of conversion at 1100 °C for aluminum nanoparticles (Aveka Inc.), and a best fit to each reaction model. The results presented indicate that our experimental data are better fitted to the diffusion controlled model. Thus, we argue that two stages of reaction take place for aluminum nanoparticle oxidation: one where the shell of the aluminum oxide layer is quickly formed followed by the condensed phase diffusion limited reaction. Once the very thin surface layer is formed, the kinetics would then be controlled by diffusion.

These results enable us to calculate the effective diffusion coefficients of oxygen through the ash layer using the rate constant as shown in Eq. 14, to give $D_e = 1.07*10^{-9}$ (600 °C) ~ $1.31*10^{-8}$ (900 °C) cm^2/s for DC arc generated aluminum nanoparticles of ~50 nm (i.e., $D_e = D_0 \exp(-E_a / RT)$ where $D_0 = 1.72*10^{-5}$ cm^2/s and E_a = 69.5 kJ/mol over 600 ~ 900 °C). To provide a more physical picture of the reactivity of nanoparticles, we compare the measured rate with the oxygen gas-collision rate [1] (i.e., the fastest possible oxidation rate).

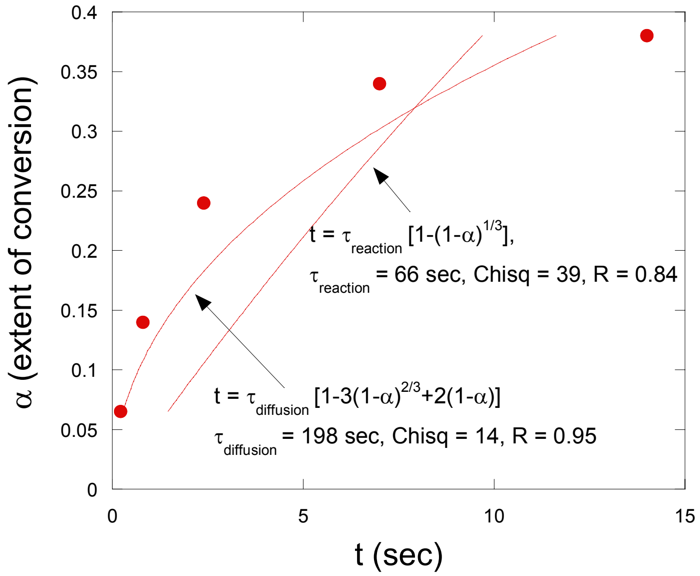

Figure 14. The reaction time (t) and extent of conversion at 1100 °C for aluminum nanoparticles (Aveka Inc.) with the fitted lines determined by diffusion-controlled and chemical reaction-controlled shrinking core models.

Theoretical collision rate (molecules/sec) = $\dfrac{P_{O_2}\pi D_p^2}{(2\pi m k_b T)^{1/2}}$

Measured reaction rate (molecules/sec) = $-\dfrac{dN_{O_2}}{dt} = \dfrac{4\pi D_e}{\left(\dfrac{1}{r_c}-\dfrac{1}{R}\right)} C_{O_2}$ (15)

Where PO2 is the partial pressure of oxygen in gas, m is the molecular mass of the gas molecules, kb is the Boltzmann's constant, R is the particle size, and rc is the radius of unreacted core. The theoretical collision rate at 900 oC for 50 nm particle is ~3.0*1012 molecules/sec, which is much greater than our experimental value (~7.4*105 molecules/sec).

3.3. Characterization of Metal-Containing Diesel-Emitted Particles

Classification of Particles and Size Distributions for their Classes

In this section, we would like to address the final application of single particle mass spectrometry to obtain the size- and composition- resolved statistics needed to gain insight into the formation mechanisms of metal-bearing diesel particles, for the full size range of diesel particulate matters (DPM). [12,15] For the experiment, a Isuzu diesel engine is operated at high or low engine load and with or without adding ppm levels of the ferrocene to the diesel fuel as a source of metal (Fe), the emitted DPM is sampled approximately isokinetically from the tailpipe and then fed into the SPMS as usual. Also DPM samples are taken for TEM/EDS analysis using a low-pressure cascade impactor (LPI). [37] Together with TEM/EDS observation, the particle mass spectra are sorted into the following basic classes or particle types.

1. “Elemental Carbon (EC)” particles, are defined as those where H/C < 1. These are particles containing greater relative amounts of elemental carbon (typically agglomerates of primary carbon spherules).
2. “Organic Carbon (OC)” particles are defined as those where H/C >1. They are typically nanoparticles containing fuel or oil residues rich in organic carbon i.e. rich in hydrogen.
3. “Pure iron” particles, are those where Fe/C > 10. These are the nanoparticles of iron (presumably self nucleated in the engine).

The values of C, H and Fe are molar ratios and obtained from the corresponding peak areas in the individual mass spectra. Thousands of particle mass spectra are collected and analyzed to divide the particles into the classes. DPM in each class is then sorted and binned according to size. Before looking at detailed particle stoichiometry, we present for these three particle types the frequency distribution of each type as a function of particle size. As an example, Fig. 15 shows the number-weighted mobility size distributions for each of the three particle types at two different engine conditions and high (200 ppm) doping rates of iron. The EC particles are widely distributed in size, with a peak at around 70 nm, and constitute the bulk of the particulate material, which coincides with the size distribution of agglomerate particles measured by SMPS. The figure also shows that the OC particles are distributed in the lower size range (< 50 nm). At low engine load, we see virtually no “pure iron” particles. This is probably due to higher carbon generation at low load (characteristic of this particular engine), preferentially facilitating Fe adsorption onto carbon particles rather than nucleation of Fe.

At high engine load, the increase in Fe throughput combined with inherent soot reduction yields a higher Fe/C ratio, so the pure iron particles have increased in number and grown in size to a point where the aerodynamic lens is able to transmit them more efficiently to the ionization laser in the SPMS. Fig 15(b) shows that about 9% of the detected particles (by number) are pure iron nanoparticles. Note that in this figure the size distribution of the elemental carbon particles has not changed significantly, which is consistent with the SMPS measurement.

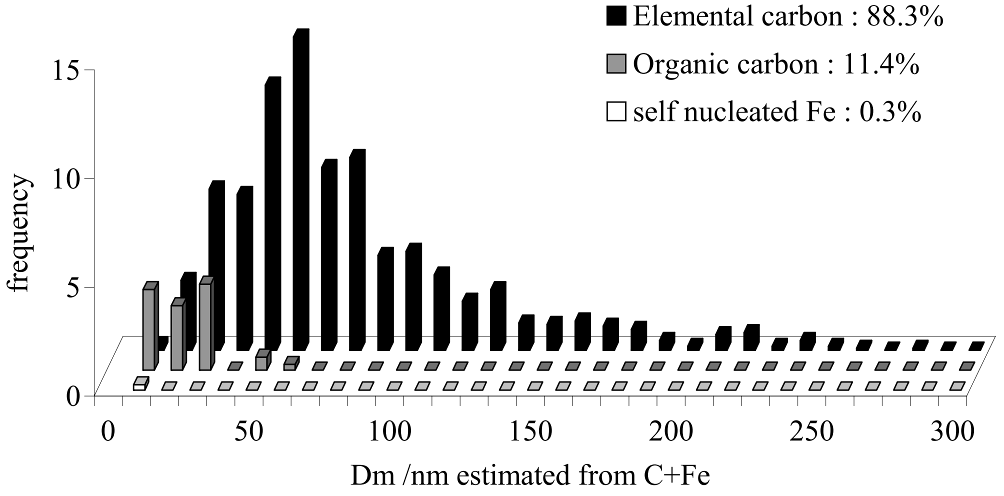

a)

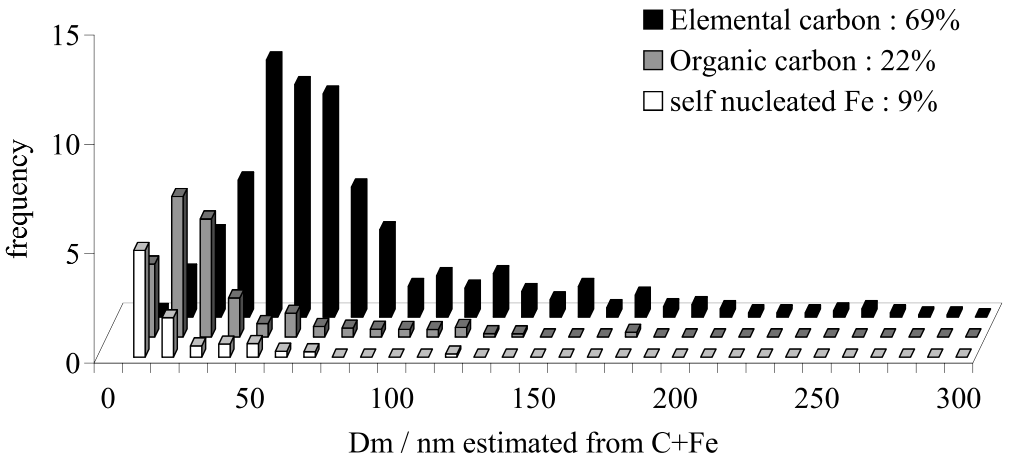

b)

Figure 15. Size distributions for three classes of diesel exhaust particles with high-Fe doping: (a) 0kW load, (b) 6kW load. Note that percent distributions refer to frequency of occurrence.

Mechanism of Particle Formation

We observe in Fig. 16 that the H/C ratios are clearly greater for smaller particles, but the scatter in the data demonstrates how elusive it would be to define a “typical” H/C ratio for diesel particles. The variation in H/C may reflect the locally varied temperature history that the particles underwent, which results in local variation in the (partial) burning of fuel and lube oil, as well as variation in the vapor deposition history. The solid line in Fig. 16 is drawn to indicate that the amount of hydrocarbon deposited to the preexisting iron-bearing carbon particles scales as D_m^2, i.e. approximately to the surface area of the accumulation mode PM. This might imply that a significant portion of the volatile hydrocarbon condenses near the tail pipe where exhaust gas containing volatile hydrocarbon is cooled. Under those conditions the very small sized PM would undergo free-molecular condensation, i.e. where condensation rate is proportional to the surface area of particle cores. Note that the horizontal axis in the figures corresponds to mobility size of composite particles estimated from the sum of carbon and iron peak areas.

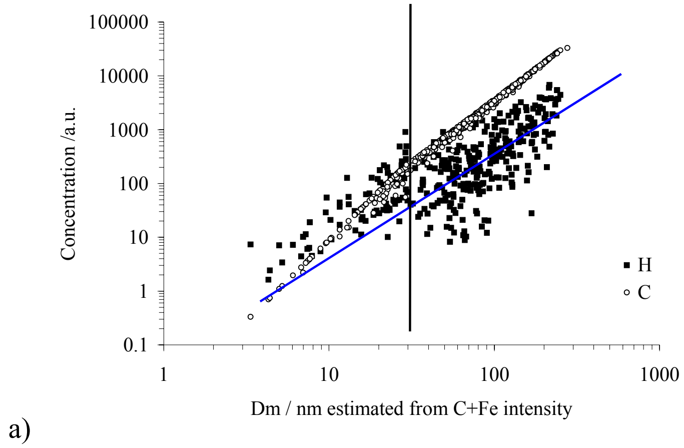

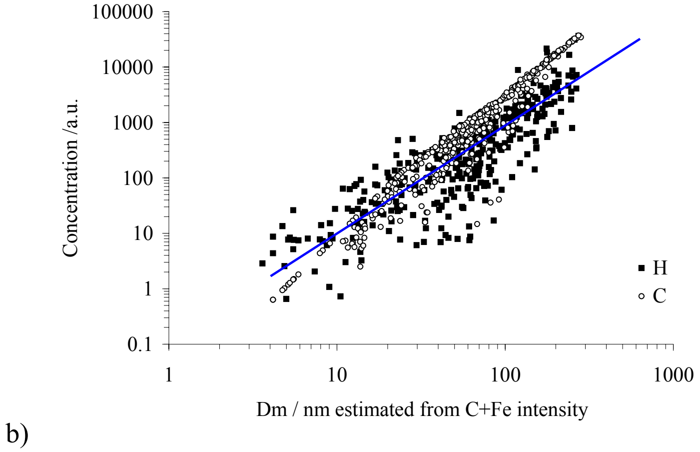

Figure 16. Size dependence of carbon and hydrogen in diesel exhaust particles for the case of high-Fe doping: (a) 0W load, (b) 6kW load. (Note: solid line through data shows $D_{m,c}^2$ dependence of elemental concentration).

Next, we are going to talk about the formation of iron species in DPM. For our experiment, high engine load conditions result in increased fuel flow rate i.e. to run the engine at constant speed as engine load increases. The quantity of Fe more than doubles due to this increased fuel flow rate, while the soot concentration decreases, due to improved fuel-air ratio at high load (for this engine) and to the soot suppression effect of metals [38-40]. The combined effect heightens the Fe/C ratio, effectively increasing the super-saturation ratio of iron vapor in the combustion chamber, in turn causing the nuclei mode particles to grow larger and more numerous. This is best seen in Fig. 17 (a-b), which show that for the 200 ppm doping rate, the higher Fe throughput at high engine load results in increased iron levels for the especially small particles. Note that at the low engine load (Fig. 17a) the data shows a tightly banded distribution of iron and a relatively low iron fraction over much of the particle size range i.e. lower engine loads produce less iron relative to carbon because the engine produces more carbon and less fuel is consumed to provide iron. In comparison, Fig. 17b shows that at higher engine load, many of the smaller particles lie above the carbon curve, suggesting they are “pure iron” particles, while many of the larger particles have iron content similar to the low load case. Overall, the relative amount of Fe is also higher and more variable over the entire size range for the high load case. The latter can be explained by the dominance of mutual coagulation i.e. over nucleation and condensation, between the three types of particles.

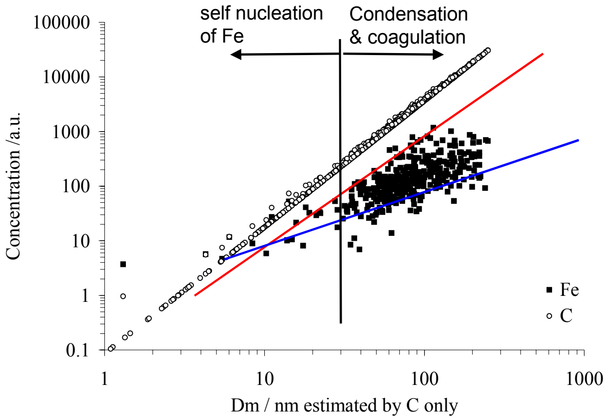

a)

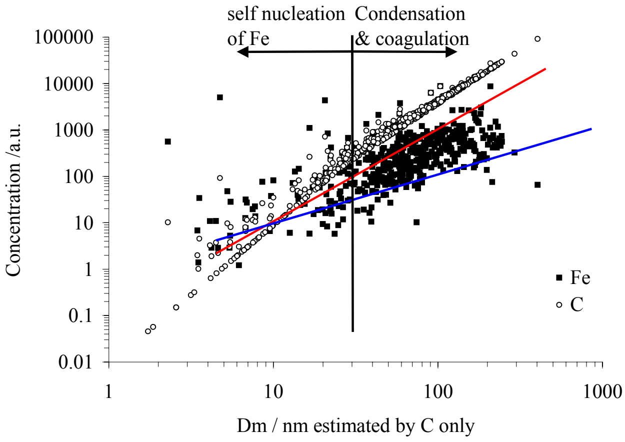

b)

Figure 17. Size dependence of iron and carbon fractions in diesel exhaust particles for the case of high-Fe doping: (a) 0W load, (b) 6kW load. (Note that upper line shows $D_{m,c}^2$ while lower line shows $D_{m,c}^1$).

Note that in Fig. 17a-b, the mobility size corresponds to carbon core mobility diameter that is estimated from the carbon peak area only. We postulated that the iron is condensed to the preexisting carbon core or self-nucleate inside the engine cylinder due to its very low vapor pressure. If this is the case, the behavior of particles may lie in the continuum regime, for which the deposition rate of Fe is proportional to diameter. [1] The slope of the plotted data Fe vs $D_{m,c}$ lies indeed between lower and upper solid lines representing continuum and free molecular regime, respectively, which is obviously smaller than the slope of H vs D_m in

Fig. 16. This is not surprising because inside the engine the pressure is very high, moving the particle behavior toward continuum conditions, where the deposition rate of Fe is proportional to $D_{m,c}$.

4. DEVELOPMENT OF SINGLE PARTICLE MASS SPECTROMETRY

In this section we describe two new developments which are aimed at further improving the SPMS performance. In Sections II-5, we reported that significant particle size-dependent ion loss occurs prior to detection in conventional single particles mass spectrometry. This leads to increasing the lowest limit of particle mass measurement and more seriously to significant errors in the measured chemical composition of core-shell structured nanoparticles. In order to confirm the structural effect, similar method was applied for multi-component particles with two distinct structures such as light absorbing Al or Al_2O_3 particle coated with transparent NaCl and a mixture particle of those species. [41], We found that the core Al fraction of the core-shell particle is unlike the well mixed composite particles or pure salt. To prevent it, we need to develop a new type of ion optics in order to make the detection efficiency (DE) defined in Section II-5 to be KE invariant. In other words, the sloping DE versus KE profile should be flattened as suggested by lines A or B in Fig. 7. The second new development addresses the limitations of entraining and detecting ultrafine particles. To investigate ultrafine environmental aerosols one needs a well-designed aerodynamic lens to tightly focus and deliver the particles into the ionization laser focus. The narrower the focused aerosol beam, the more chance the laser has of hitting the particles, which becomes very important for ultrafine particles. In this regard, we acknowledge that two key elements, i.e. improved aerodynamic lens and ion optics characterize the uniqueness of our current SPMS. In this section, we would like to describe our efforts to progressively develop the best designs for those features.

4.1. Design of a New Ion Optics

Before addressing the design, we would like to mention that every ion optics system has a certain KE window of energetic ions to be measured. The objective of our design approach is to find a way to minimize ion losses by assessing and optimizing the KE of the ions. We first measured the maximum KE of the ions generated in the SPMS seen in Fig. 1. The upper limit is determined to be 200eV by estimating the initial KE of an ion from the peak width at the baseline of the mass spectrum. On the basis of the ion trajectories in the conventional ion optics as seen in Fig. 6, we used ion tracing software to evaluate several design trials including the curvature of the ion repelling plate, the addition of an Einzel lens, the use of a tubular electrode, and combinations of these.

Trial 1: Curved Repelling Plate

Observing the ion trajectories in Fig. 6, we are intuitively aware that diverging ion trajectories are compressed more if the configuration of the repelling plate is bent like a concave plane. As the first trial, a new repelling plate with various parabolic curvatures is applied (mathematical equation for parabola $y^2 = 4px$). A parabolic plate with greater curvature, such as a concave mirror, deflects ions more effectively than a less parabolic plate including a flat plate as seen in Fig. 18. This is because the curvature generates an electrical repulsion force that is expected to collapse the conical ion beam to the centerline by parallelizing equipotential lines to the curved electrode. The origin of the conical ion beam is located in the middle of the vertex (x=0) which coincides with center of the extraction grid where the ionization laser is fired. At a fixed repelling voltage, greater curvature of the plate clearly improves the ion focusing, but not enough to completely parallelize the beam (the meaning of this will be explained later). Furthermore, at p = 10, a number of ions are slightly overfocused, as highlighted with a dotted oval. When the curvature is increased further, the overfocusing becomes greater, leading to less detection efficiency. Also it is not possible to use such a repelling plate for the SPMS without drilling holes through which both laser and aerosol beams penetrate.

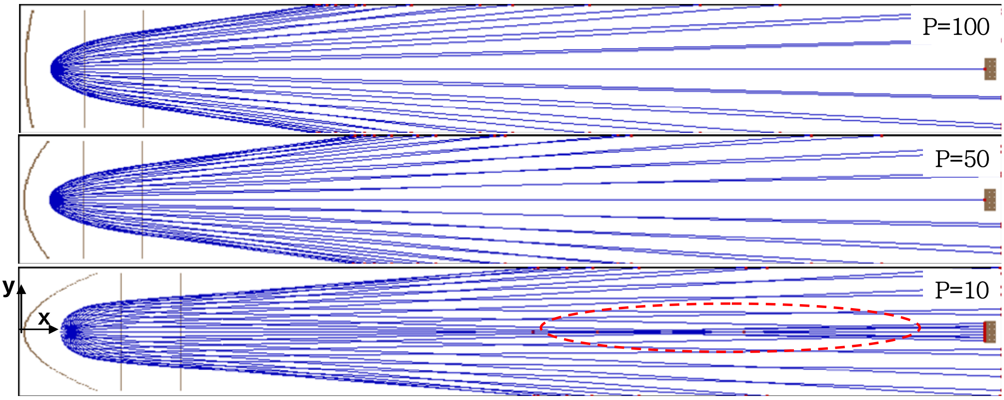

Figure 18. Curvature effect of the repeller plate on the ion trajectories at KE=100eV; the rectangle at the right end represents a MCP detector with an aperture of 18mm. The voltages for the three electrodes are V_R=4500V, V_E=3350V, and V_R=0V from the left.

Trial 2: Einzel Lens

Our next attempt to reduce ion losses entails employing an Einzel lens consisting of three cylindrical tubes. The first and the third tubes are electrically grounded while the central tube, which is equidistant from the first and the third ones, is held at a positive voltage as seen in Fig. 19. The incident ions are first decelerated and then accelerated. At the same time, they begin to move to the centerline of the TOF tube. Thus, the ion beam can be focused by using this lens system without imparting any net acceleration to the ions. For parallel-incident ions, the higher the KE of the ions, the longer the focal length of the lens becomes. Even with higher electrode voltage, confocal focusing of incident ions with different kinetic energies has never been achieved, though the focal length is shortened for all kinetic energies.

Taking a closer look at Fig. 19, it is observed that ions approaching far from the centerline of the lens are overfocused quicker than those closer to the centerline. In contrast, an Einzel lens both ends of which are bonded with fine metallic nets certainly helps to reduce the length of the focusing zone, as noted by "L_f" in the figure, which becomes closer to what is known as confocal focusing. The former problem provides an important clue in the resolution of that problem. If it is possible to position easily focusable (less energetic) ions close to the centerline and more energetic ions near the inner surface of the tube before their incidence, ions with different KEs are likely to be focused at the nearly the same position. As shown in Fig. 6, conventional ion optics essentially produces a conical ion beam the width of which is proportional to the ion KE. More energetic ions intrinsically fly into the Einzel lens farther from the centerline, which is desirable for the confocal focusing. In order to realize this result for the SPMS, it is necessary to make all incident ion trajectories parallel to the central axis before the entrance to the Einzel lens, which is the only remaining problem.

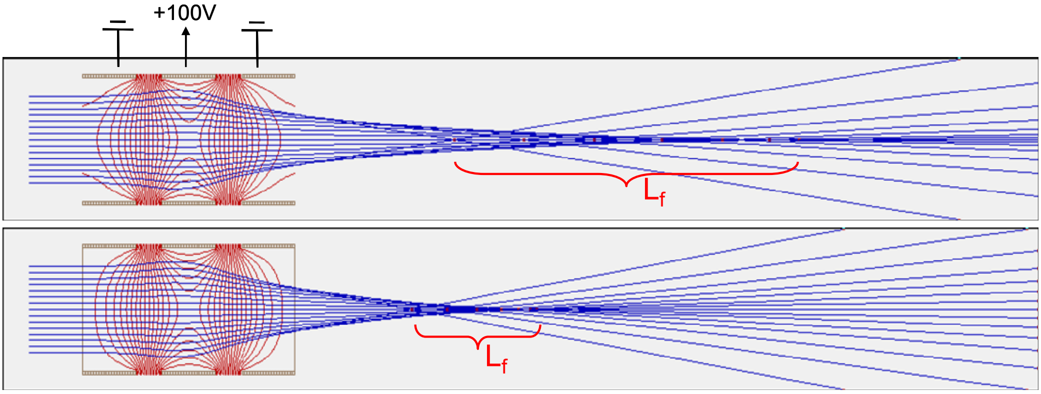

Figure 19. Comparison between (a) a conventional Einzel lens with (b) a lens with a grid for focusing of the incident ion beams at KE = 150eV; L_f represents a focusing zone over which each focal point of ions entering at different radial positions is distributed. Blue and red lines are ion trajectories and isopotential lines, respectively. The diameter and length of each tube are 16mm and 10mm, respectively.

Trial 3: A Tubular Electrode and the Final Design

The third trial would be to locate some type of effective deflector downstream of, but as close as possible to, the extraction grid. One of the best candidates would be the Einzel lens, but it is typically as long as ~ 15 mm. A shorter Einzel lens with a strengthened lens-deflection capability as a strong deflector is needed. Noting the benefit of the Einzel lens with two nets, we propose to insert a tubular electrode between the first and second grid electrodes in Fig. 1. This results in a new minimized assembly including an ion repelling plate and a focusing device. This is termed a “tubular electrode assembly (TEA)”, throughout this article. Fig. 20 shows that the TEA deflects ion trajectories progressively with increase in the voltage (V_T) of the tubular electrode, eventually making the trajectories parallel to the TOF axis.

However, the distance between the laser focus and the detector appears to be too short for proper digitization of ion signals. Therefore, an additional Einzel lens is located downstream of the TEA so as to focus ion trajectories to the detector with a diameter of 18mm at the end of the 1-m long TOF tube. A three-dimensional configuration of the complete ion optics is described with dimensions of its components in Fig. 21. The figure confirms that 0-200 eV energetic ions are detected with a repelling voltage as low as 7000V, the typical voltage used for the SPMS.

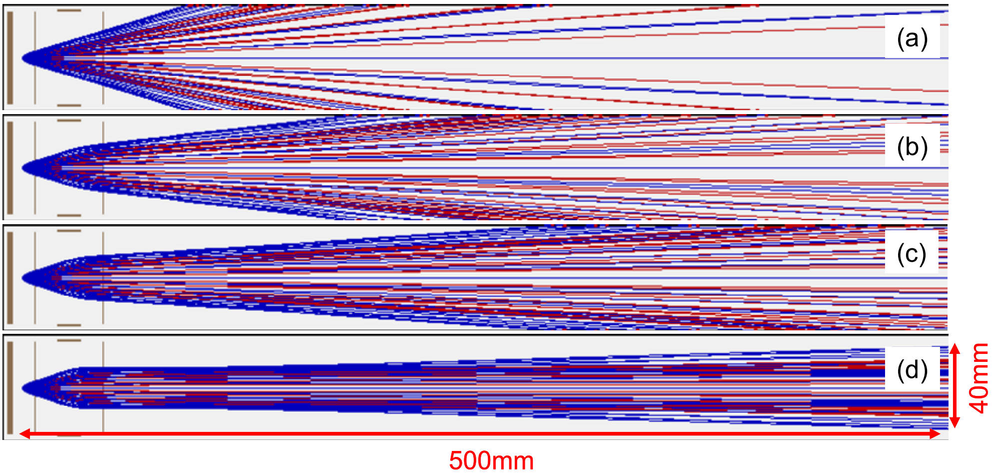

Figure 20. Characteristics of the tubular electrode assembly comprised of blue and red lines corresponding respectively to KE = 200 and 100eV. The voltages to the tubular electrode are altered at (a) 0V, (b) 2000V, (c) 2500V and (d) 3000V, maintaining a repeller plate voltage constant at 4500V together with two grounded grids. The red and blue lines represent ion trajectories at KE = 100 and 200eV, respectively.

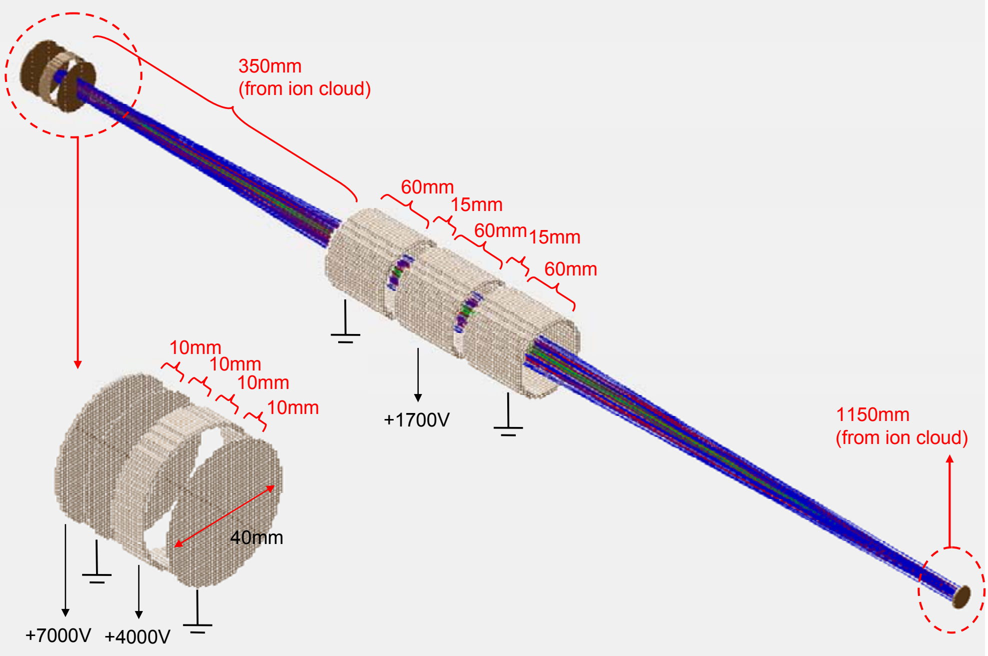

Figure 21. Development of a new ion optics consisting of a tubular electrode assembly and an Einzel lens for 100% detection of 0 – 200eV energetic ions; the MCP detector with an effective size of 18mm is shown as a disc at the right end. The green, red and blue lines correspond to KE = 10, 100 and 200eV, respectively.

4.2. Design of an Aerodynamic Lens

To evaluate and optimize entrainment and focusing of the inlet particle beam, numerical simulation is performed to track particle behavior by utilizing FLUENT software (version 6.2.16). Under typical operating condition of the aerodynamic lens (ADL) inlet for the SPMS, particle concentration is so low that inter-particle interaction is negligible and the existence of particles hardly affect the gas flow. [42-45] Therefore, particle-free gas flow is first calculated under the assumption of axisymmetric, steady, compressible, laminar and viscous flow. Then particles with a specified diameter are launched at various radial positions in the simulated gas flow field. The particles in the present simulation are assumed to be spherical NaCl particles with a density of ~ 2 g/cc. By solving the Langevin equation including inertia and drag forces [42-46], we could simulate particle trajectories through the ADL system. As the particle size of interest in this study ranges from 30 to 300 nm, we don't include in the calculation the Brownian motion of particles that would have a significant effect especially for the size smaller than 30 nm. [45]

Analysis of Single Aerodynamic Lens

The performance of the ADL or the single lens has been often represented by overall contraction ratio (ηc) of particle beam and transmission efficiency (ηt) of particles. The two factors have been expressed as a function of four dimensionless groups [42-46], i.e. df/OD, L/df, flow Reynolds number (Re0) based on OD and particle Stokes number (St) as

$$\begin{aligned} \eta_c &= f(d_f / OD, L / d_f, \mathrm{Re}_0, St) \\ \eta_t &= g(d_f / OD, L / d_f, \mathrm{Re}_0, St) \end{aligned} \qquad (16)$$

Due to the low pressure inside the ADL, the gas mean free path is much larger than 300 nm, leading the particle behavior to the free molecular regime. In that regime, the St can be defined using Epstein's mobility as: [44,46]

$$St = \frac{1}{\left(1+\frac{\pi\alpha}{8}\right)\sqrt{2\pi\gamma^3}} \frac{\dot{m}\rho_p d_p c^3}{p_{up}^2 d_f^3} \propto \frac{\rho_p d_p}{p_{up}^2 d_f^3 M^{3/2}} \qquad (17)$$

where α is the momentum accommodation coefficient (close to the unity), γ is the specific heat ratio of the gas (1.4 for air), ρp is particle density, dp is particle diameter, $\mathrm{c} = \sqrt{\gamma \mathrm{RT}_{\mathrm{up}} / \mathrm{M}}$ is the speed of sound in the gas at the upstream temperature (Tup). M is molecular weight of the gas and $\dot{\mathrm{m}}$ is mass flow rate of carrier gas, respectively. Notably, Eq 17 implies that the St has a functional dependence on the systematic parameters of dp, df, pup and M. Since the Re0 can not vary even at different dfs where flow characteristics are significantly different, the gas flow should be better characterized by the other Reynolds number based on the df rather than the OD as

$$\mathrm{Re} = \frac{\rho V d_f}{\mu} = \frac{4\dot{m}}{\pi \mu d_f} \propto \frac{1}{d_f} \tag{18}$$

where μ is gas viscosity that does not depend on the pressure. The mass flow rate $\dot{m}$ is not varied much from a typical value of 0.0026 g/s (125sccm) under the current operating condition of the SPMS. Also from mass conservation, $\dot{m}$ is treated as constant throughout this article unless otherwise stated. If the df decreases, the Re and St are both increased (see Eqs 17-18), leading to significant changes in both gas flow characteristics and particle behavior. At the same time, the Pup is expected to increase too because the downstream pressure is fixed constant in the operation of the SPMS. The higher Pup condition reduces the detrimental effect of particle diffusion. More importantly, as the OD is often restricted geometrically for the application to the SPMS, the lens-geometry-related parameter (df/OD) would be reduced into the Re (see Eq 18). The length of spacer L is not a big concern for the design as long as the L is long enough for the gas flow to redevelop after the orifice. Taking these issues into account, Eq 16 is likely reduced to the simpler form as

$$\eta_c = f(\mathrm{Re}, \mathrm{St}),\ \eta_t = g(\mathrm{Re}, \mathrm{St}) \tag{19}$$

At the fixed df where Re is constant (see Eq 18), the ηc must be determined solely by the St. Indeed, Zhang et al.'s simulation [42,43] obviously shows that the curves of the ηc against dp or Pup fall into a single curve of ηc versus St (see Figures 7-8 and Figure 14 in references Zhang et al. [42] and Zhang et al. [43], respectively). Moreover, this implies that there should exist an optimal Stokes number (St0 when ηc = 0) for best focusing aerosols with optimal particle size (dp0). As seen in Fig. 22, particles smaller than the dp0 are not efficiently focused while larger particles (> dp0) are overfocused due to their greater inertia. Rearranging Eq 17 for df, one can estimate the optimal size (df0) of single orifice so as to focus particles with a specified size of dp0 as [44]

$$d_{f0} = \frac{1}{\left(1+\frac{\pi\alpha}{8}\right)^{1/3} \left(2\pi\gamma^3\right)^{1/6}} \left(\frac{\dot{m}\rho_p d_{p0} c^3}{p_{up}^2 St_0} \right)^{1/3} \tag{20}$$

Analysis of Multi-Lens System

Using Eq 20, we first determine the opening sizes of five successive lenses so that each lens is designed to focus particles with a particular dp0. The present ADL system obtained in this way shows that the df0 decreases gradually in the streamwise direction. This means that the expected optimal sizes (dp0) of particles decrease in that direction, because the dp0 is mainly proportional to df03 as long as the St0 does not change much (see Eq 17 or 20). But, the universal optimal Stokes number St0 (at ηc = 0) exists only when the Re is not varied along all orifices (see Eq 19). This would be true only in the case of using same-size lenses in series which is known to be less effective.

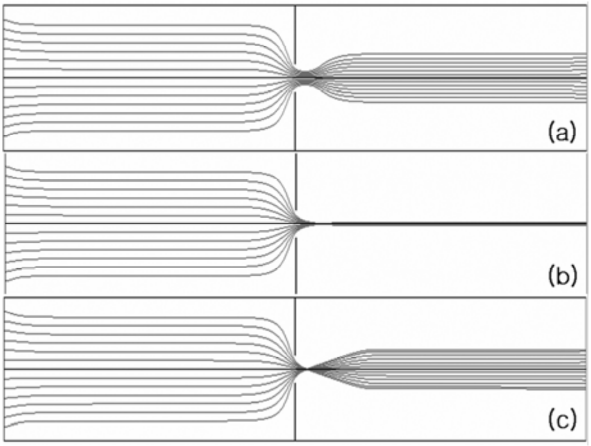

Figure 22. Particle size-dependent focusing of single lens: (a) insufficient focusing smaller particles (d_p=30nm), (b) focusing intermediate sized particles (d_p=150nm), (c) overfocusing larger particles (d_p=500nm) : Q = 125sccm.

In our multi-lens system seen in Fig. 23, Re and St are both drastically increasing along the lenses. Eq 19 indicates that ηc vs St curves at different Reynolds numbers will not collapse into a single line, which is qualitatively consistent with Zhang et al.'s finding [42] from single lens analysis (refer to Figures 9-11 in reference Zhang et al. [42]). As the universality of the St0 is broken in our multi-lens system and the Pup experiences a stepwise decrease to the stable low pressure downstream, the optimal size of particles at each stage of the multi-lens system would deviate from that expected by Eq 20. Hence, one may have to know the St0 at each stage in the whole system, prior to the determination of the orifice diameters. This would be tedious time-consuming iterations of initial guess of df0s and numerical simulation for the whole system. Liu et al. [46] reported that when df/OD < 0.25, the St0 has a weak dependence on the ratio. In Zhang et al.'s design [43] where the ratio varies from 0.4 to 0.5, the St0 is very sensitive to the ratio as confirmed by their simulation. Recalling our inference that the effect of the ratio could be interpreted as another effect of the Re (see the pre-mentioned discussion on Eq 4), it is not a surprise to see a strong dependence of the St0 on the Re. [43] In contrast, Wang et al.'s ADL system [45] with the ratios of 0.17 - 0.27 showed that the St0 had a very weak dependence on the Re (see Figure 2 in reference).

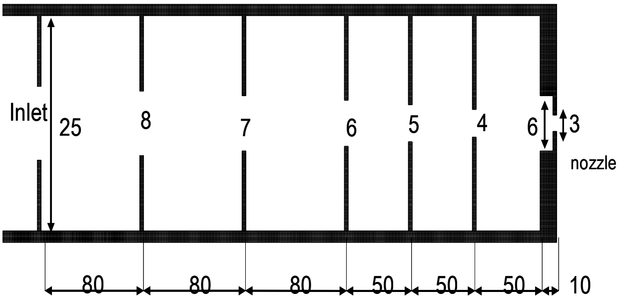

Figure 23. Schematic of an aerodynamic lens designed to focus 30-300nm aerosols. The geometric dimensions are in mm.

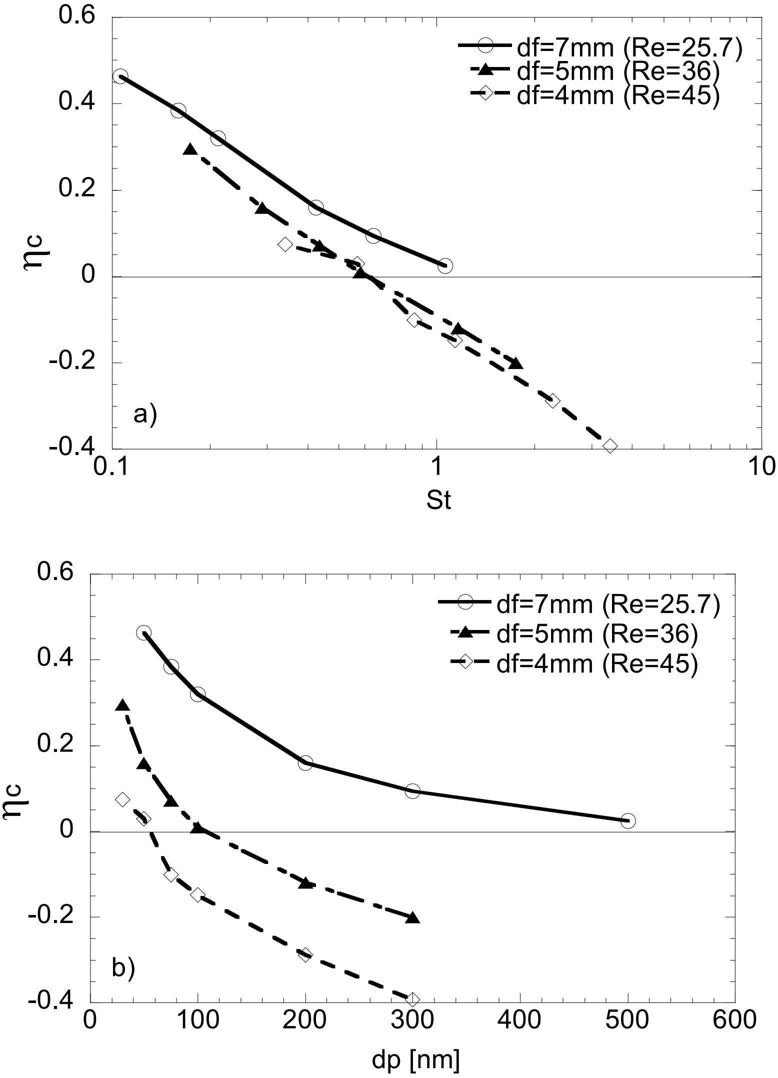

Figure 24. Comparisons of contraction ratios at the 2nd, 4th and 5th lenses as a function of (a) Stokes numbers and (b) particle diameters : Q = 125sccm.

Interestingly, Fig. 24(a) shows that the St0 is not varied around 0.6 from the 3th orifice to nozzle. But, the 1st and 2nd orifice diameters give the ratio of 0.32 and 0.28, respectively, which are slightly larger than the critical value of 0.25 by Liu et al. [46]. Therefore, the universality of the St0 is slightly broken only at these two orifices, moving the St0 to 1.0.

We listed in Table 4 optimal particle sizes (dp0) at each orifice and nozzle for both the optimal Stokes numbers of 0.6 and 1.0. As the Re = 22 at the 1st orifice is pretty close to that at the 2nd orifice, it should be a reasonable approximation to use St0 = 1.0 for the 1st orifice. The optimal particle sizes predicted for the orifices are highlighted with a bold style in the table. The result indicates that the present ADL system is designed for focusing nanoparticles in a wide range of 15 – 700 nm.

Table 4. Comparisons of design parameters between the present design and the previous ones at Q = 125 sccm.

OD[mm] = 25							
lens order	df	df/OD	Ma	Re	Pup[Pa]	dpo[nm]	Sto
1	8	0.32	0.086	22.48	227.2	750	1.036
2	7	0.28	0.112	25.69	225.6	390	0.816
3	6	0.24	0.155	29.97	223.2	210	0.713
4	5	0.2	0.228	35.97	218.6	105	0.642
5	4	0.16	0.386	44.96	209.2	43	0.561

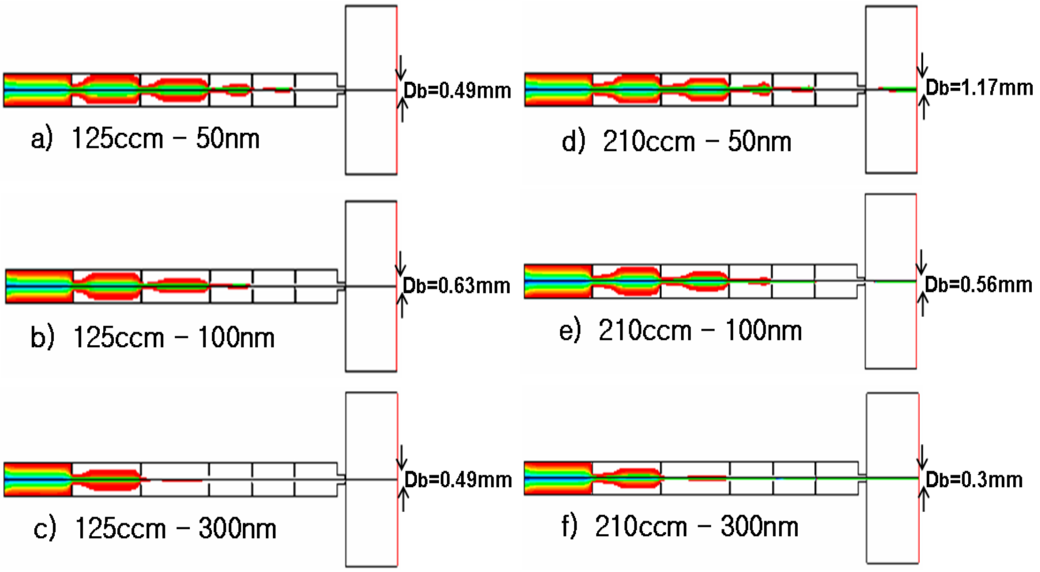

Figure 25. Trajectories of particles with a variety of their sizes at two gas flow rates.

In addition, we consider two aerosol-gas flow rates of 125 and 210 sccm upstream of the flow limiting orifice. The use of a smaller mass flow rate or a smaller flow limiting orifice provides an advantage of focusing smaller particles because it decreases all upstream pressures inside the ADL and thereby the St for the smaller particle increases in the direction of approaching the St0. But, this is achieved at the expense of the hitting rate of aerosols by the SPMS. Fig. 25 presents the trajectories of aerosol particles of 50, 100, and 300 nm together with the final aerosol beam diameters 40mm downstream of the ADL exit. Fig. 25(a) shows 50 nm particles are collimated at the 5th nozzle, which is exactly identical to the predicted location in Table 4. Both the figure and table show that particles of dp0 = 300 nm are completely focused between the 2nd and 3rd orifices. We would like to emphasize that the final beam diameters is still in the sub-millimeter range.

CONCLUSIONS

In this article, we offered a broad review for single particle mass spectrometry, starting from the working principle and several concerns for interpretation of the data, through applications to probe nanoscale phenomena, to introduction of some ideas for better design, based on our previous publications on the SPMS. There are a couple of other historical review articles dealing with the application i.e. investigation of accumulate-mode environmental aerosols using aerosol time-of-flight mass spectrometry. However, this article is specifically devoted to explaining the whole process including initial approach, theory, and experimental evaluation for each topic. We hope that this will provide some guideline for readers who are interested in the use and/or the development of the SPMS in the field of nanoparticle technology.

ACKNOWLEDGMENTS

This work was supported by Core Environmental Technology Development Project for the Next Generation (Project No. 102-071-058).

REFERENCES

[1] Friedlander, *S. K. Smoke, Dust*, and Haze; John Wiley & Sons: New York, 1977.
[2] Kodas, T.; Hampden-Smith, *M. Aerosol Processing of Materials*; Wiley: New York, 1999.
[3] Ivanov, G. V.; Tepper, F. *4th International Symposium on Special Topics in Chemical Propulsion*. 1997, 636.
[4] Aumann, C. E.; Skofronick, G. L.; Martin, J. A. J. Vac. *Sci. Technol*. B. 1995, 13 (3), 1178.
[5] Ortega, A. *Int. J. Chem. Kinetics*. 2001, 33, 343.
[6] Mahadevan, R.; Lee, D.; Sakurai H.; Zachariah, *M. R. J. Phys. Chem.* A. 2002, 106, 11083-11092.
[7] Kittelson, D. J. *Aerosol Sci*. 1998, 29, 575-588.
[8] Gross, D. S.; Galli, M. E.; Silva, P. J.; Wood, S. H.; Liu, D. -Y.; Prather, *K. A. Aerosol Sci. Technol.* 2000, 32, 152-163.
[9] Noble, C. A.; Prather, *K. A. Mass Spectrum. Rev*. 2000, 19, 248-274.
[10] Park, K.; Lee, D.; Rai, A.; Mckherjee, D.; Zachariah, *M. R. J. Phys. Chem. B*. 2005, 109, 7290-7299.
[11] Rai, A.; Lee, D.; Park, K.; Zachariah, *M. R. J. Phys. Chem. B*. 2004, 108, 14793-14795.
[12] Lee, D.; Miller, A.; Kittelson, D.; Zachariah, *M. R. J. Aerosol Sci*. 2006, 37, 88-110.
[13] Lee, D.; Miller, A.; Park, K.; Zachariah, *M. R. Int. J. Automotive Technol*. 2006, 7(6), 667-673.
[14] Lee, D.; Park, K.; Zachariah, *M. R. Aerosol Sci. Technol*. 2005, 39, 162-169.
[15] Lee, D.; Cho, S.-W.; Lee, S. G.; *Kim, S.-G.. J. Korean Phys. Soc*. 2006, 49(1), 370-375.
[16] Cho, S.-W.; Lee, *D. Rapid Commun. Mass Spectrom*. 2007, 21(20), 3286-3294.
[17] Lee, K.-S.; Cho, S.-W.; *Lee, D. J. Aerosol Sci*. 2008, in press.

[18] Johnston, *M. V. J. Mass Spectrom*. 2000, 35, 585-595.

[19] Salt, K.; Noble, C. A.; Prather*, K. A. Anal. Chem*. 1996, 68, 230.

[20] Refer to the manual of the ATOFMS available at *http://www.tsi.com*.

[21] Reents, W. D.; *Ge, Z. Aerosol Sci. Technol*. 2000, 33, 122-134.

[22] Reents, W. D.; Schabel, *M. J. Anal. Chem*. 2001, 73, 5403-5414.

[23] Lee, S. G.; Choi, S. M.; Lee, *D. Thermochimica Acta*. 2007, 455(1-2), 138-147.

[24] Smith, R. A.; Tisch, J. W. G.; Ditmire, T.; Springate, E.; Hay, N.; Mason, M. B.; Gumbrell, E. T.; Comley, A. J.; Mountford, L. C.; Marangos, J. P.; Hutchinson, *M. H. R. Phys. Scripta*. 1999, T80, 35-39.

[25] Last, I.; Jortner, *J. Phys. Rev. Lett*. 2001, 87, 033401.

[26] Ditmire, T.; Donnelly, T.; Rubenchik, A. M.; Falcone, R. W.; Perry, *M. D. Phys. Rev*. A. 1996, 53, 3379.

[27] Hutchinson, M. H. R.;, Ditmire, T.; Springate, E.; Tisch, J. W. G.; Shao, Y. L.; Mason, M. B.; Hay, N.; Marangos, *J. P. Phil. Trans. R. Soc. Lond. A*. 1998, 356, 297.

[28] Chen, Z. Y.; Cogley, C. D.; Hendricks, J. H.; May, B. D.; Castleman, *A. W. J. Chem. Phys*. 1990, 93, 3215.

[29] Snodgrass, J. T.; Roehl, C. M.; Bowers, *M. T. Chem. Phys. Lett*. 1989, 159, 10.

[30] McPherson, A.; Luk, T. S.; Thompson, B. D.; Borisov, O. B.; Shiryaev, O. B.; Chen, X.; Boyer, K.; Rhodes, *C. K. Phys. Rev*. Lett. 1994, 72, 1810.

[31] Milchberg, H. M.; McNaught, S. J. et al. *Phys. Rev*. E. 2001, 64(5-2), 056402.

[32] Zhou, L.; Park, K.; Milchberg, H. M.; Zachariah, *M. R. Aerosol Sci. Technol*. 2007, 41, 818.

[33] Vyazovkin, S.; Wight, *C. A. Int. Rev. Phys. Chem*. 1998, 17, 407.

[34] Brown, M. E. *Introduction to Thermal Analysis Techniques and Applications;* Chapman and Hall: London, 1988.

[35] Ettarh, C.; Galwey, *A. K. Thermochimica Acta*. 1996, 288, 203.

[36] Levenspiel, *O. Chemical Reaction Engineering; 3rd ed*.; John Wiley & Sons: 1999.

[37] Hering, S.; Friedlander, S.; Collins, J.; Richards, *W. Environ. Sci. Technol*. 1979, 13(2):184-188.

[38] Miyamoto, N.; Zhixin, H.; Harada, A.; Ogawa, H.; *Murayama, T. SAE Papers* 871612. 1987, 1-7.

[39] Bonczyk, *P. A. Comb. Flame*. 1991, 87, 233-244.

[40] Otto, K; Sieg, M. H.; Zinbo, M.; Bartosiewicz, L. SAE Papers. 800336. 1980, 277-289.

[41] Zhou, L.; Rai, A.; Zachariah, *M. R. Int. J. Mass Spectrom*. 2006, 258, 104.

[42] Zhang, X.; Smith, K. A.; Worsnop, D. R.; Jimenez, J.; Jayne, J. T.; Kolb, *C. E. Aerosol Sci. Technol.* 2002, 36, 617-631.

[43] Zhang, K.; Smith, K. A.; Worsnop, D. R.; Jimenez, J. L.; Jayne, J. T.,; Kolb, C. E.; Morris, J.; Davidovits, *P. Aerosol Sci. Technol*. 2004, 38, 619-638.

[44] Wang, X.; Kruis, F. E.; McMury*, P. H. Aerosol Sci. Technol*. 2005a, 39, 611-623.

[45] Wang, X.; Gidwani, A.; Girshick, S. L.; *McMurry, P. H. Aerosol Sci. Technol*. 2005b, 39, 624-636.

[46] Liu, P.; Ziemann, P. J.; Kittelson, D. B.; McMurry, *P. H. Aerosol Sci. Technol.* 1995a, 22, 293-313.

[47] Wang, X.; McMurry, *P. H. Int. J. Mass Spectrom*. 2006, 258, 30-36.